Exciton Confinement in Natural Quantum Wells and Subwavelength Focusing Using a Negative Refractive Index Slab

by

Benjamin P. Isaacoff

A thesis submitted in partial fulfillment
of the requirements for the degree of
Honors Bachelor of Science
(Physics)
in The University of Michigan
2012

Advisor:

Professor Roberto Merlin

Banksy in Timbuktu, 2008.

Even a zebra needs help maintaining its stripes.

ACKNOWLEDGEMENTS

This work was only made possible thanks to my advisor, Professor Roberto Merlin. I will forever be grateful that he saw the potential in me as a young student and allowed me to be a part of his group for these past three years. He has been a constant source of guidance and help, both scientifically and personally, and I truly feel prepared to go on to the next step in my career as a scientist, largely thanks to this experience.

I must also thank my fellow group members: Andrea Bianchini, Ilya Vugmeyster, Lei Jiang, Jingjing Li, Prashant Padmanabhan, Alex Toulouse, Steve Young, Greg Affeldt, Meredith Henstridge, and Ibrahim Boulares for their constant help, advice, and friendship. I am especially indebted to Alex, who has been my partner for the work on excitons; he has been a great friend and mentor, helping me navigate these past few years and showing me the finer points of careful experimentation.

I could never have gotten to this point without the unwavering love and support of my friends and family. I am especially grateful to my parents who instilled a deep curiosity in me at a young age. My girlfriend Nichole has given me the love and support of ten people, and I know that any success I have achieved thus far has been made possible by having her as my partner. I am incredibly fortunate to have had so many wonderful people in my life, the great majority of whom have gone unnamed here, and I will always be grateful for their contributions in the past and for those yet to come.

TABLE OF CONTENTS

ACKNOWLEDGEMENTS ii

LIST OF FIGURES v

CHAPTER

I. Exciton Confinement in Atomically Thin GaSe & PbI_2 Natural Quantum Wells 1

1.1 Excitons and Confinement 2
1.1.1 Excitons 3
1.1.2 Confinement effects 5
1.2 GaSe & PbI_2 8
1.2.1 Crystal Structure 8
1.2.2 Optical Properties 10
1.3 Sample Preparation and Identification 13
1.3.1 Sample Preparation 13
1.3.2 Sample Identification 14
1.4 Measurements 18
1.4.1 Reflection Experiment 18
1.4.2 Atomic force microscopy 22
1.5 Results and Interpretation 23
1.6 Conclusions and Further Work 27

II. Numerical and Analytical Analysis of Subwavelength Focusing Using a Negative Refractive Index Slab 29

2.1 Geometry 29
2.2 Point Dipole Source 30
2.2.1 Source Field 30
2.2.2 Transverse Decomposition of Source Field 32
2.2.3 Derivation of Transmission Functions 33
2.2.4 Construction of the Transmitted Field 35
2.2.5 Analysis of the Transmitted Field 38

2.3 Line Dipole Source 43
2.3.1 Source Field 43
2.3.2 Construction of the Transmitted Field 44
2.3.3 Analysis of the Transmitted Field 57
2.3.4 Lossless case 58
2.3.5 Comparison with Numerical Results 62
2.4 Conclusion 63

APPENDICES 65

BIBLIOGRAPHY 71

LIST OF FIGURES

Figure

1.1	Exciton absorption peaks in ultrapure GaAs at 1.2 K, from [9] . . .	4
1.2	Exciton absoprtion in GaAs, left to right at 294 K, 185 K, 90 K, and 21 K, from [9] . . .	5
1.3	Illustration of a semiconductor/dielectric heterostructure. Left: a single layer of active region. Right: a layered structure with multiple active regions . . .	7
1.4	Absorption spectra showing exciton peaks taken at 2 K of 4000, 210, and 140 Å thick GaAs layers between $Al_{0.2}Ga_{0.8}As$ barriers, from [10]	8
1.5	Perspective and top views of a unit layer of GaSe in the ϵ polytype, from [12] . . .	9
1.6	Perspective view of PbI_2, the iodine atoms are black and the lead atoms are white, from [14] . . .	10
1.7	Temperature dependence of E_g of GaSe, from [15] . . .	11
1.8	Absorption coefficient of GaSe at various temperatures. (1) T = 290 K, (2) 175 K, and (3) 70 K, from [16] . . .	11
1.9	Temperature dependence of E_g of PbI_2. The squares are experimentally determined, the dashed lines give the error range, and the solid line is the fit, from [17] . . .	12
1.10	Absorption coefficient of PbI_2, at T = 4.5 K and T = 77 K, from [18]	13
1.11	(Left) Bulk single crystal of PbI_2 (Right) Peeled PbI_2 on scotch tape	14
1.12	Peeled PbI_2 on a Si substrate . . .	15
1.13	Contrast of monolayer of GaSe illuminated with light λ on Si wafer with oxide thickness d . . .	16
1.14	Magnitude of the contrast for various thicknesses of GaSe flakes as a function of wavelength λ on Si wafer with oxide thickness 285 nm .	17
1.15	A typical sample with a distribution of thickness of PbI_2 flakes on a Si wafer . . .	17
1.16	A diagram showing our reflection measurement setup. . . .	19
1.17	An illustration showing what we view in real time using the camera, the red arrow points to the white spot which is the focused measurement beam . . .	20

1.18 (Left) an optical image of a GaSe flake (Right) An AFM scan of the same sample . . . 23
1.19 Adding a Lorentzian and a parabola can produce very different looking backgrounds . . . 24
1.20 Reflection spectrum of a bulk (~ 70 μm) piece of PbI_2 . . . 25
1.21 Reflection spectra of very thin PbI_2 flakes, the thickness of the sample is indicated on the plot . . . 26
1.22 Reflection spectra of a 14 nm thick PbI_2 flake, one of the thinest we have measured. . . . 27
2.1 The geometry being considered, where the region $0 \leq z \leq d$ is occupied by a left-handed material with permitivity and permeability $\epsilon = -1 + \delta\epsilon$ and $\mu = -1 + \delta\mu$. The regions $z < 0$ and $z > d$ are vacuum. . . . 30
2.2 (Left) Density Plot and (Right) 3D Plot of $|\mathbf{H}_t|$ in the focal plane z=$\frac{3}{2}d$ 40
2.3 The z dependence of the transmitted field for the point source geometry, the dashed line shows the focal plane of $z = \frac{3}{2}d$. (Left) $\ln|\mathbf{H}_t|$ (Right) $|\mathbf{H}_t(z,x)/\max[[\mathbf{H}_t(z)]]|^2$ . . . 40
2.4 $|\mathbf{H}_t|$ in the focal plane $z = \frac{3}{2}d$. Top row, left to right, $\theta_P = 90°, 60°, 45°$, and in the bottom row, left to right $\theta_P = 30°, 0°$ . . . 41
2.5 Comparison of the numerically calculated resolution length with (2.32) as a function of $\delta\epsilon$ . . . 42
2.6 The z dependence of the transmitted field for the line source geometry, the dashed line shows the focal plane of $z = \frac{3}{2}d$. (Left) $\ln|\mathbf{H}_t^{NF}|$ (Right) $|\mathbf{H}_t^{NF}(z,x)/\mathbf{H}_t^{NF}(z,0)|^2$ . . . 57
2.7 Typical field profile of $|\mathbf{H}_t^{NF}|$ in the focal plane of $z = \frac{3}{2}d$ . . . 58
2.8 Typical field profile as a function of (z,x), the dashed line indicates the focal plane of $z = \frac{3}{2}d$. Left: $\ln|\mathbf{H}_t^{NF}|$ Right: $|\mathbf{H}_t^{NF}(z,x)/\mathbf{H}_t^{NF}(z,0)|^2$ 61
2.9 Typical field profile of $|\mathbf{H}_t^{NF}|$ in the focal plane of $z = \frac{3}{2}d$ . . . 61
2.10 Comparison of $|\mathbf{H}_t^{NF}|$ for the lossy case calculated analytically and numerically, Left and Right respetivley . . . 63
2.11 Comparison of $|\mathbf{H}_t^{NF}|$ for the lossless case calculated analytically and numerically, Left and Right respetivley . . . 63

CHAPTER I

Exciton Confinement in Atomically Thin GaSe & PbI_2 Natural Quantum Wells

Graphene, the monolayer of graphite that is one atom thick and produced in a pencil trace, has grabbed the attention and sparked the imagination of scientists and engineers around the world. Graphene was first isolated and studied in 2004 by Geim and Novoselov [1], who were subsequently awarded the 2010 Nobel Prize in Physics for showing it to be the first truly two-dimensional material. Due to its reduced dimensionality, graphene exhibits a wide range of amazing properties that have led to countless applications [2]. Graphene has many superlatives to its name–it is the thinnest and the strongest material ever studied [3]. Its carriers are massless quasi relativistic particles that exhibit the largest mobility of any known material [4]. It has been proposed to use graphene to usher in the post Si computing era, to create flexible high speed electronics, to create sensors with single molecule sensitivity, to create composite materials with unprecedented properties, and a limitless number of other applications [5]. Graphene is a wonder material that has proved to be one of the most interesting materials ever studied.

Motivated by the incredible properties of graphene and with the new knowledge that atomically thin crystals can exist and are thermodynamically stable, we set out to isolate and study atomically thin sheets of a layered semiconductor. Furthermore,

we wanted to study how reducing the dimensionality of these crystals affected the behavior of neutral electron-hole bound pairs, called excitons. This was in part motivated by a long tradition of studying excitons in epitaxially grown quantum well systems [6]. This previous work and our own expectations indicated that by following the simple procedure pioneered in the discovery of graphene [1], we would be able to reach thicknesses that would allow us to measure effects due to quantum confinement. We were also hopeful that this system would allow us to gain some insight into the long standing problem of an additional electromagnetic boundary condition for exciton-polaritons, first pointed out by Pekar in 1958 [7].

We have isolated atomically thin sheets of the layered semiconductors gallium selenide (GaSe) and lead (II) iodide (PbI_2). We have optically studied the excitons in these materials and observed some effects consistent with our expectations of exciton confinement. In this chapter, I will first give a brief introduction to excitons and confinement effects. I will then detail the sample preparation and identification methods used. I will explain our measurements and present some results. Finally I will give a brief overview of our current interpretation, and the further work that needs to be done.

1.1 Excitons and Confinement

In this section I will give a very brief and simplified overview of excitons and confinement effects. By no measure will this be exhaustive or comprehensive, it is only intended to give enough background in order to understand the basic theory behind our experiment. The interested reader can consult any of a number of relevant textbooks for a more thorough background.

1.1.1 Excitons

Excitons are neutral electron-hole bound pairs, which can be treated as a quasi-particle and can be produced in many different kinds of systems; I will restrict my attention here to excitons in semiconductors. When light of high enough energy is incident on a semiconductor, it can promote an electron to the conduction band, leaving behind a positively charged hole in the valence band. Due to their close spatial proximity, the Coulomb attraction between the electron and hole can cause them to attract each other, and if bound properly, form an exciton. Excitons share a lot of similarities to positronium or hydrogen, and it is often helpful to visualize them as such by substituting the hole for the positron or proton. In semiconductors, we are mainly concerned with free excitons, also called Wannier-Mott excitons. Free excitons are called such because they are spatially delocalized states which extend throughout many lattice spacings and can move freely throughout the crystal.

To rigorously solve for the energies of the exciton bound states would be a lengthy quantum mechanical calculation; instead, we will rely on the Bohr model and effective mass theory, which is a well-documented and useful approximation [8]. Furthermore, because the exciton radius may be many lattice spacings, we also will use effective medium theory and treat the material as a uniform dielectric. Defining the reduced electron-hole mass as $\mu = (1/m_e^* + 1/m_h^*)^{-1}$, where m_e^* and m_h^* are the electron and hole effective masses respectively, we can write the energy levels of the exciton [9] as:

$$E(n) = -\frac{\mu R_H}{m_0 \epsilon_r^2 n^2} = -\frac{R_X}{n^2} \tag{1.1}$$

Where R_H is the Rydberg constant for Hydrogen, m_0 is the electron mass, and ϵ_r is relative dielectric constant. I have introduced R_X as the exciton Rydberg constant.

Due to the Coulomb attraction, the energy required to create an exciton is slightly lower than the energy normally required to create an electron-hole pair, the bandgap

energy E_g. Thus the energy of the exciton will be

$$E_n = E_g - \frac{R_X}{n^2} \tag{1.2}$$

Therefore, because it is energetically favorable to produce excitons at energies slightly below the bandgap, we expect peaks in absorption near the band-edge, corresponding to the creation of excitons. Fig. 1.1 shows the $n = 1, 2, 3$ exciton peaks in GaAs.

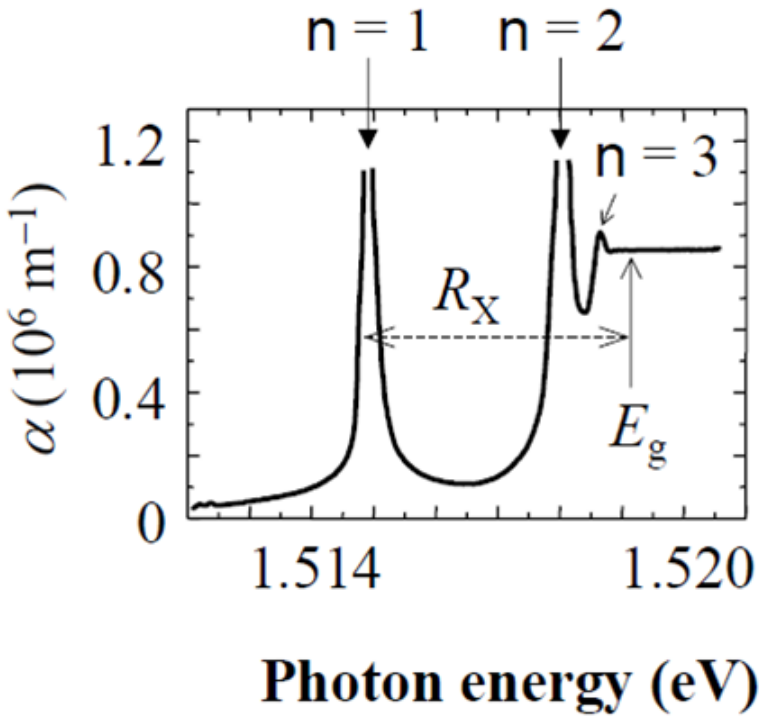

Figure 1.1: Exciton absorption peaks in ultrapure GaAs at 1.2 K, from [9]

Free excitons typically have lifetimes on the order of picoseconds to nanoseconds. One of the main modes of exciton dissociation that we can control for is collisions with phonons. The maximum energy of a thermally excited phonon in the high temperature limit is $E \approx k_b T$, k_b being Boltzmann's constant. Therefore in order to have more long-lived excitons we want $k_b T \ll E_n$. This results in exciton absorption peaks begin much sharper and taller at lower temperatures. Fig. 1.2 shows absorption near the gap for GaAs at various temperatures; remember that E_g is also a function

of temperature. Therefore, in order to have more long-lived excitons, we want the

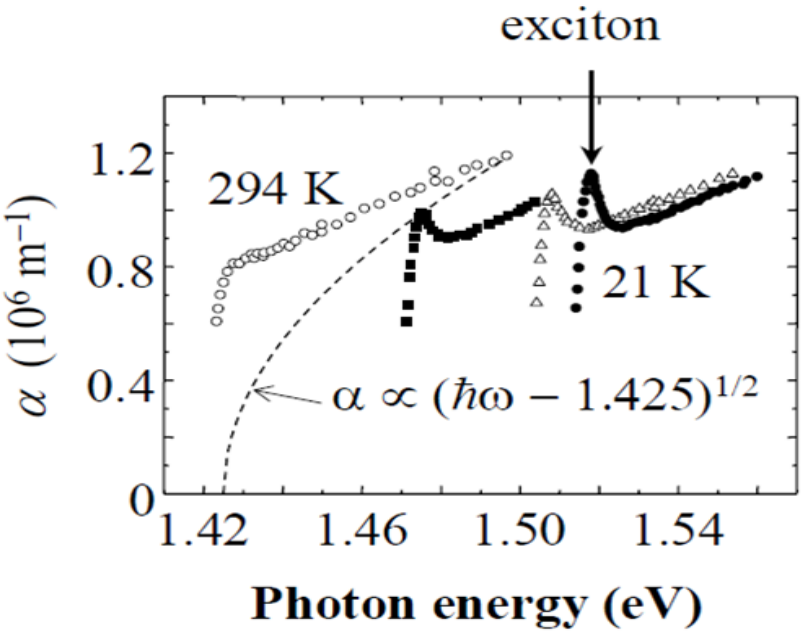

Figure 1.2: Exciton absoprtion in GaAs, left to right at 294 K, 185 K, 90 K, and 21 K, from [9]

binding energy of the exciton to be greater than the thermal energy. For this reason, all of our experiments thus far have been conducted at 77 K, but we will soon move to 4 K to better resolve the exciton.

1.1.2 Confinement effects

Confinement is when we restrict the number of free dimensions of a particle. Confinement effects show up often in quantum mechanics and electromagnetism. One of the easiest ways to see that confinement has far reaching implications is to simply use the Heisenberg uncertainty principle $\Delta x \Delta p \geq \hbar/2$, which means that a particle's momentum can take on a much greater range of values for smaller Δx. More specifically, when a particle's DeBroglie wavelength is on the order of one of the dimensions clearly there will be confinement effects. Thanks to the long history of studying epitaxially grown 2-D semiconductor quantum wells, we had some expectations about

the kind of effects we should see.

It turns out that one can predict a lot about *real* quantum wells by studying an idealized infinite square well. The confinement in a quantum well causes the wavefunctions in the direction of the well to assume stationary states of the potential, and the energy to form quantized levels in the direction of confinement. The particles are free to move in the plane of the well, and their wavefunctions must satisfy the time-independent Schrödinger Equation in three dimensions:

$$\frac{-\hbar}{2m}\nabla^2\psi(x,y,z) + V(z)\psi(x,y,z) = E\psi(x,y,z) \tag{1.3}$$

Where the direction of confinement is taken to be $\hat{z}$, E is the energy, and $V(z) = 0$ inside the well and is infinite everywhere else. For a well of width l, the energy levels are:

$$E_n = \frac{\hbar^2\pi^2 n^2}{2ml^2} + \frac{\hbar^2(k_x^2 + k_y^2)}{2m} \tag{1.4}$$

where n is an integer corresponding to the energy level. Thus we can see that as l decreases, the energy of each individual band will increase.

As explained in Section 1.1.1, the wavefunction for free excitons typically extends through many lattice spacings. Therefore if the critical dimension aproaches the exciton radius, confinement effects will become pronounced. As the critical dimension decreases, the energies associated with confinement increase, thus adding to the exciton energy and shifting the exciton peak towards higher energies. Furthermore, because both the electron and the hole become more localized as the critical dimension decreases, the Coulomb attraction, and thus the exciton binding energy, will increase. Because the binding energy increases, the higher order excitons will become more pronounced. Also drawing an analogy to the square well, the density of states becomes quantized and one sees higher energy bandgap like jumps in the absorption, at each of these new gaps an exciton may be observed. Thus if we observe higher

energy excitons it could be difficult to tell if they are the higher order excitons or quantization of the density of states.

There has been a long history of studying confinement effects using epitaxially grown heterostructures to achieve areas of interest with critical dimensions small enough to observe confinement effects [10]. This is typically done by sandwiching a

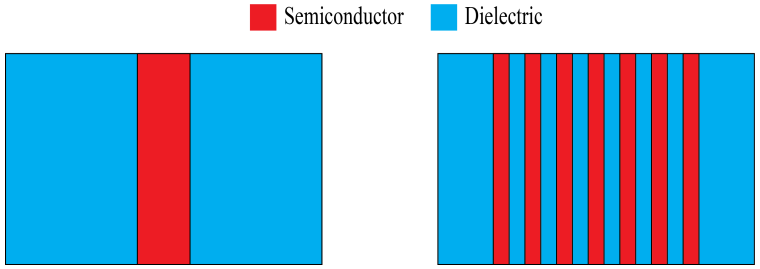

Figure 1.3: Illustration of a semiconductor/dielectric heterostructure. Left: a single layer of active region. Right: a layered structure with multiple active regions

layer of semiconductor between two layers of a dielectric, or to increase the absorption, a layered structure alternating between semiconductor and dielectric is used, as illustrated in Fig. 1.3. Much of the pioneering work done in this field was accomplished by growing GaAs/$Al_xGa_{1-x}As$ heterostructures. Fig. 1.4 shows absorption spectra showing exciton peaks for various thicknesses of GaAs active regions. Note that the $n = 1$ exciton shifts to higher energies, and the higher order excitons (or the quantization of the density of states) become visible.

In our system, which is a *natural quantum well*, we will certainly be looking for these already understood and well-established signatures of confinement effects. However, as was the lesson with graphene, a 2-D crystal is not the same as a very thin 3-D crystal. We are therefore cognizant of the posibility that new and interesting physics will be observed.

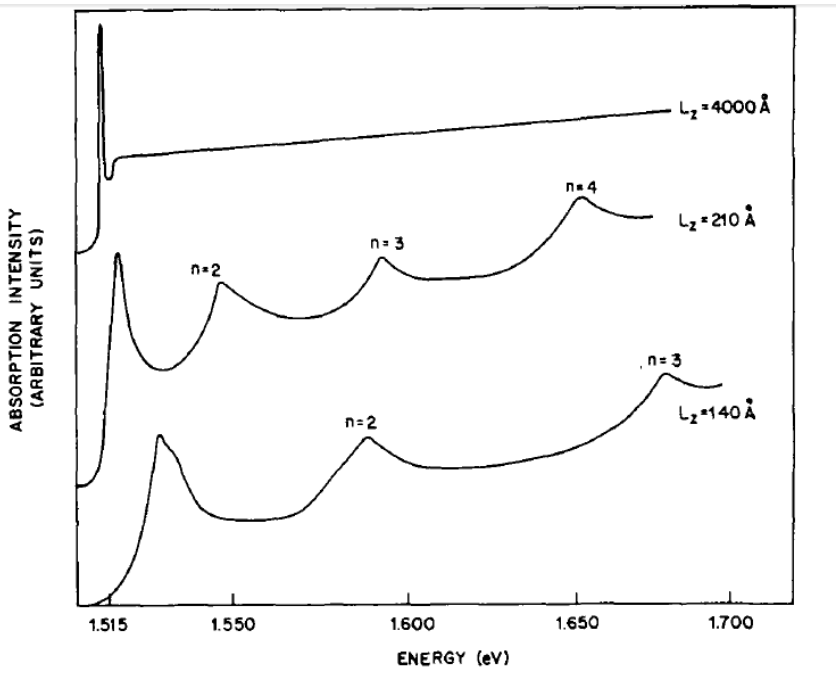

Figure 1.4: Absorption spectra showing exciton peaks taken at 2 K of 4000, 210, and 140 Å thick GaAs layers between $Al_{0.2}Ga_{0.8}As$ barriers, from [10]

1.2 GaSe & PbI_2

Our goal was to create a natural quantum well, which inspired by graphene, we hoped to make out of a few layers of a layered semiconductor. We first chose GaSe and were successful in isolating atomically thin samples. However, due to GaSe's relatively small absorption coefficient, it was difficult to resolve the exciton in extremely thin samples. We therefore switched to PbI_2, and have been more successful in studying the exciton in atomically thin samples. In this section, I will present some necessary background information about GaSe & PbI_2 that is helpful in understanding our project.

1.2.1 Crystal Structure

GaSe and PbI_2, like graphite, belong to a class of materials known as layered materials. By this I mean that they possess a layered structure with strong in-plane

bonds and a weak Van der Waals attraction between the individual layers. The much weaker inter-plane bond allows these materials to be easily cleaved and the layers to be pulled apart. This is the mechanism by which a pencil "lead", which is actually not lead at all but the layered material graphite, is able to write; when you rub the pencil lead on a surface you are shearing off layers. This has been known for quite some time and the technique utilized to produce graphene, termed micromechanical cleavage, took advantage of this property in graphite. The trick was not actually producing the monolayers, which happens when you write with a pencil, but finding them among all the other products.

GaSe comes in three different polytypes; the most common and stable polytype, and the one used in our experiment is the ϵ polytype. Henceforth, when referring to GaSe, I really mean ϵ-GaSe. GaSe crystallizes in a hexagonal structure with space group $P\underline{6}m^2$ [11]. Fig. 1.5 shows GaSe's crystal structure.

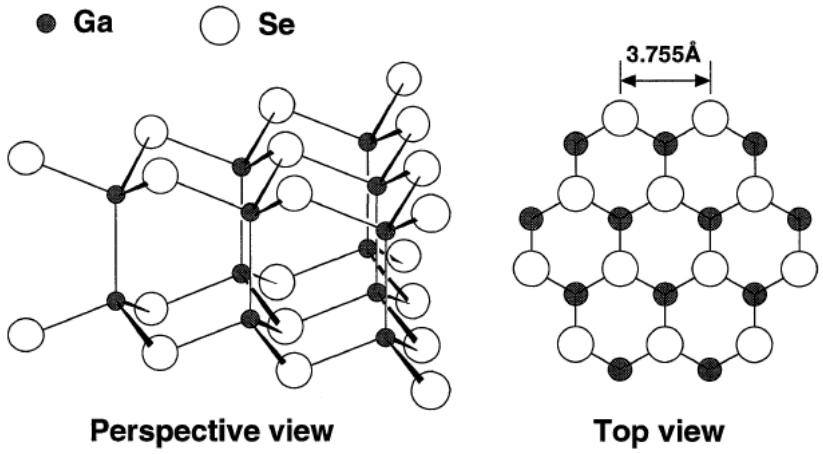

Figure 1.5: Perspective and top views of a unit layer of GaSe in the ϵ polytype, from [12]

PbI_2 also comes in polytypes. Our sample belongs to the 2H stacking sequence, where the layers stack like AcB/AcB. PbI_2 crystallizes in a hexagonal structure with space group $P\bar{3}m^1$ [13]. Fig. 1.6 shows PbI_2's crystal structure.

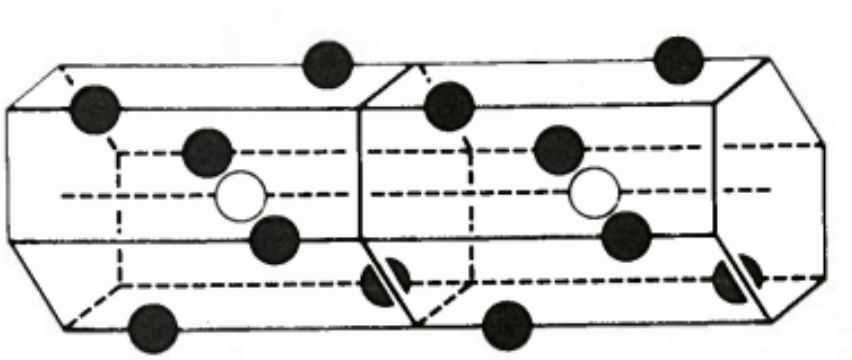

Figure 1.6: Perspective view of PbI_2, the iodine atoms are black and the lead atoms are white, from [14]

1.2.2 Optical Properties

We chose GaSe, and later PbI_2, not only because they are layered semiconductors, but also because they have prominent excitons at optical frequencies which have been studied extensively in the past. This provides us with a well understood platform from which to go forward in trying to observe new physics without having to do a lot of the background work ourselves.

As explained above, in order to better resolve the exciton, we performed most of our measurements at cryogenic temperatures, specifically at liquid nitrogen's (LN_2) boiling temperature of 77 K. Therefore, it was important for us to know how the optical properties varied with temperature. Fig. 1.7 shows the temperature dependence of the band gap energy (E_g) of GaSe as a function of temperature. The solid line has a slope of $a = (5.540 \pm 0.021) \times 10^4$ eV/K [15]. Therefore, at 77 K, $E_g \approx 2.09$ eV. Fig. 1.8 shows the absorption spectra of GaSe at various temperatures. Note that as the temperature decreases, the exciton absorption peak becomes sharper and taller, and the gap shifts towards higher energy.

The temperature dependence of E_g of PbI_2 is shown in Fig. 1.9. Note that in Fig. 1.9, they measured to lower temperatures where the trend becomes parabolic. The

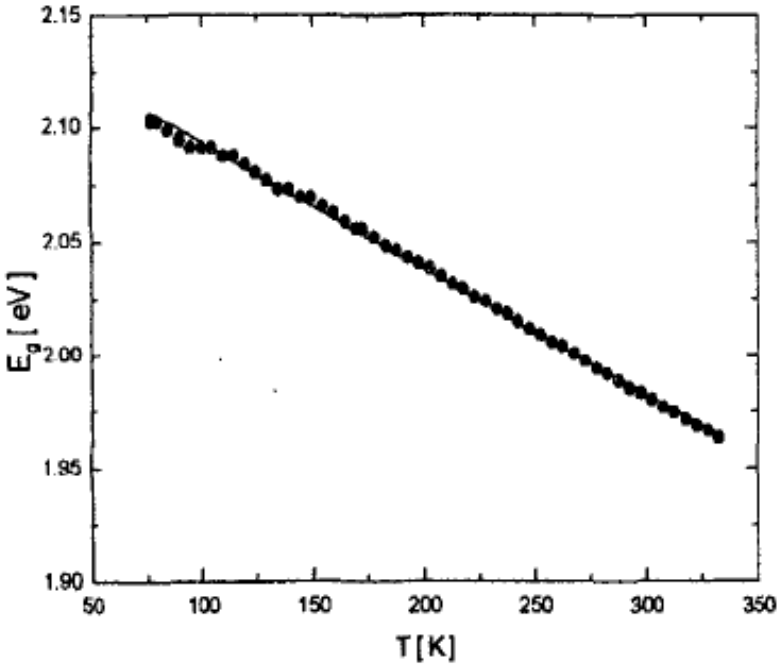

Figure 1.7: Temperature dependence of E_g of GaSe, from [15]

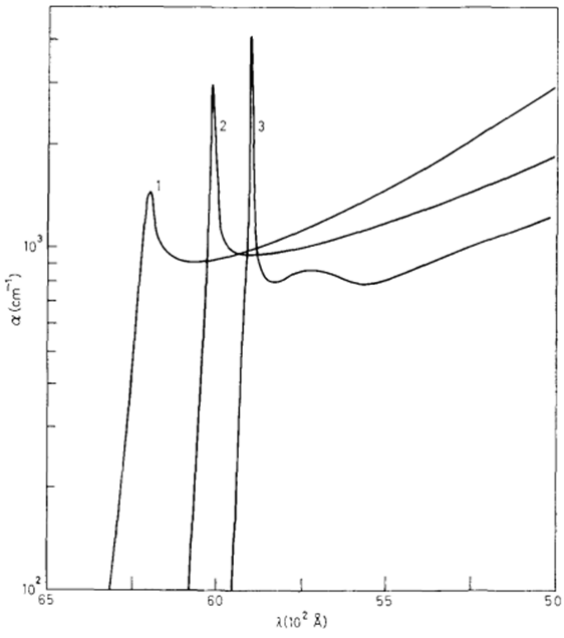

Figure 1.8: Absorption coefficient of GaSe at various temperatures. (1) T = 290 K, (2) 175 K, and (3) 70 K, from [16]

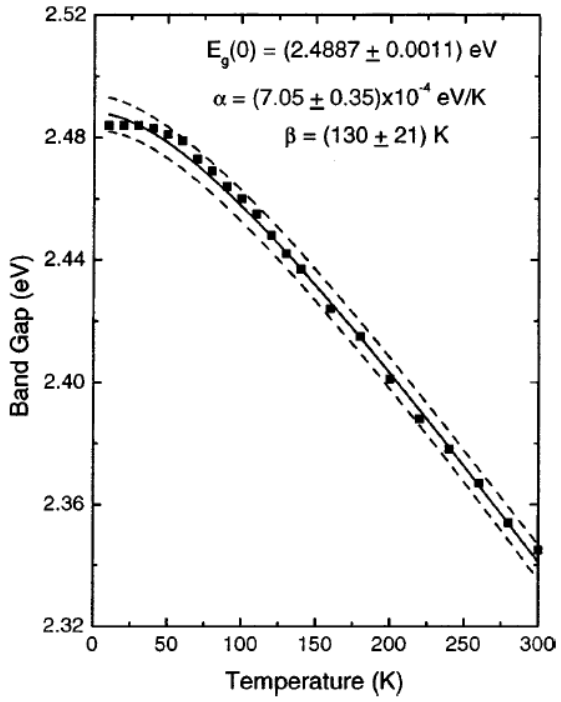

Figure 1.9: Temperature dependence of E_g of PbI_2. The squares are experimentally determined, the dashed lines give the error range, and the solid line is the fit, from [17]

fit used is [17]:

$$E_g(T) = E_g(0) - \frac{\alpha T^2}{T + \beta} \tag{1.5}$$

with the coeffecients given in Fig. 1.9. Therefore, $E_g(77) \approx 2.47$ eV. This is quite close to our experimentally determined value of $E_g(77) \approx 2.5$ eV. Fig. 1.10 shows the absorption spectra of PbI_2. Again, note that as the temperature decreases the exciton absorption peak becomes sharper and taller, and the gap shifts towards higher energy. Also by noting that the vertical axis in Fig. 1.10 is scaled by two orders of magnitude relative to Fig. 1.8, we see that PbI_2 has much stronger absorption than GaSe. This is why we decided to switch to PbI_2 from GaSe, as it allows us to resolve the exciton even in very thin samples.

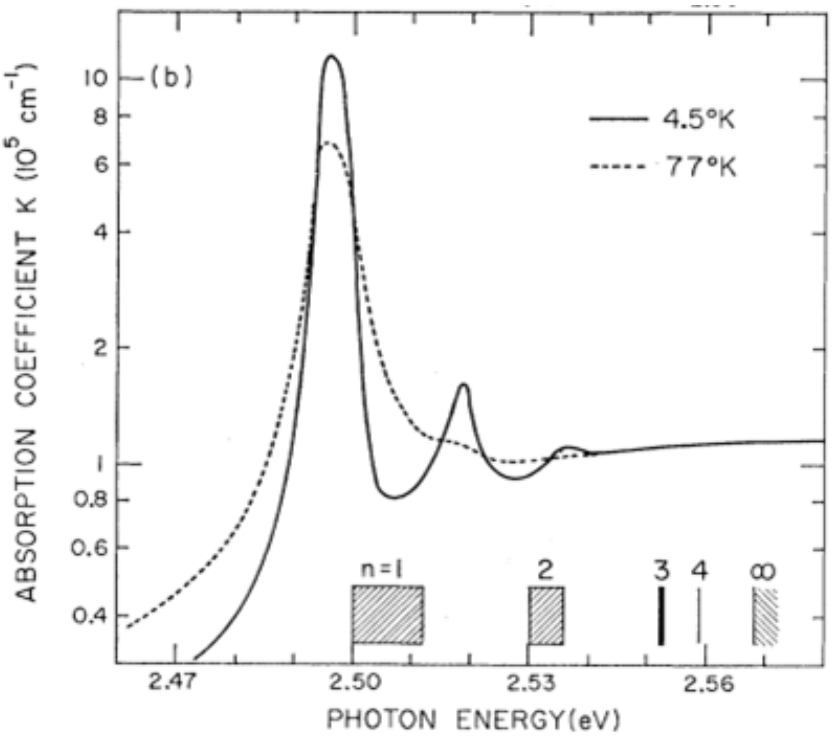

Figure 1.10: Absorption coefficient of PbI_2, at T = 4.5 K and T = 77 K, from [18]

1.3 Sample Preparation and Identification

In layered materials, the much weaker inter-plane bonding allows these materials to be easily cleaved and the layers to be pulled apart. Graphene was first isolated by repeatedly peeling graphite and optically identifying the monolayers [1]. It turns out that identifying the samples of interest is the difficult task; creating them, either with repeated peeling or some other method, is a simple task. In this section I will detail how to create the samples and how to identify the samples of interest.

1.3.1 Sample Preparation

The method used by Geim and Novoselov [1] to create graphene is often called micromechanical cleavage. This is a technical name for a process which in practice is simply repeated peeling using Scotch tape. I applied this method to GaSe and PbI_2. To accomplish this, I first begin with a suitably sized bulk piece of PbI_2 shown in

Fig. 1.11 (Left). I then peel off a small amount, usually by peeling from the top and bottom of the sample simultaneously. I then repeatedly peel that small piece, each

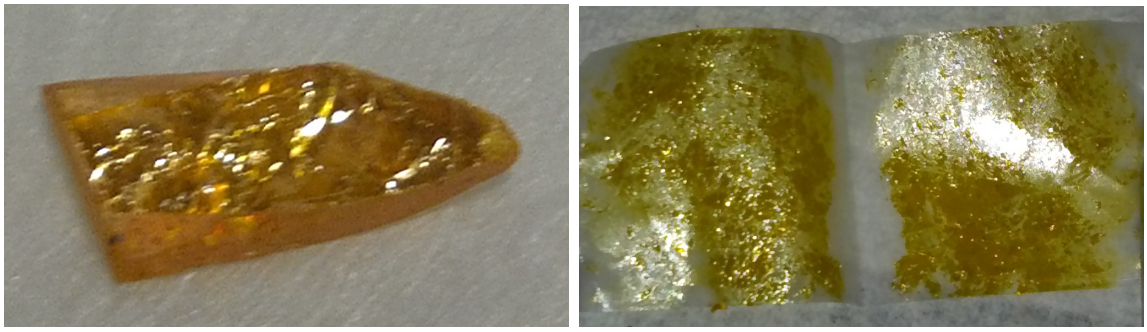

Figure 1.11: (Left) Bulk single crystal of PbI_2 (Right) Peeled PbI_2 on scotch tape

time effectively cleaving the crystal, producing thinner pieces; this is done until I have the entire area of tape covered in thin flakes of PbI_2. In the next step, I stick the tape on the surface of a pre-cut and freshly cleaned subtrate with the side of the tape that is covered in PbI_2 flakes directly in contact with the substrate. The substrate is a Si wafer with a very carefully chosen thickness of oxide. The choice of substrate is absolutely critical; this was one of the most important experimental breakthroughs in the discovery of graphene [1], which I will explain in detail in the next section. After gently rubbing the back of the tape so as to ensure that most of the PbI_2 is in direct contact with the substrate surface, the tape is peeled away. This leaves behind some of the PbI_2 flakes. Fig. 1.12 shows a picture of an entire sample with a clearly visible distribution of sizes and thicknesses of PbI_2 flakes.

1.3.2 Sample Identification

Surprisingly, a monolayer of graphene that is one atom thick, introduces a phase shift great enough that due to an optical interference, it is visible under a microscope [1]. We have found that this is also true for atomically thin GaSe and PbI_2 flakes. The source of this interference is a Fabry-Perot type of constructive intereference that occurs with the graphene flake (or GaSe or PbI_2) on top of the oxide layer, where the

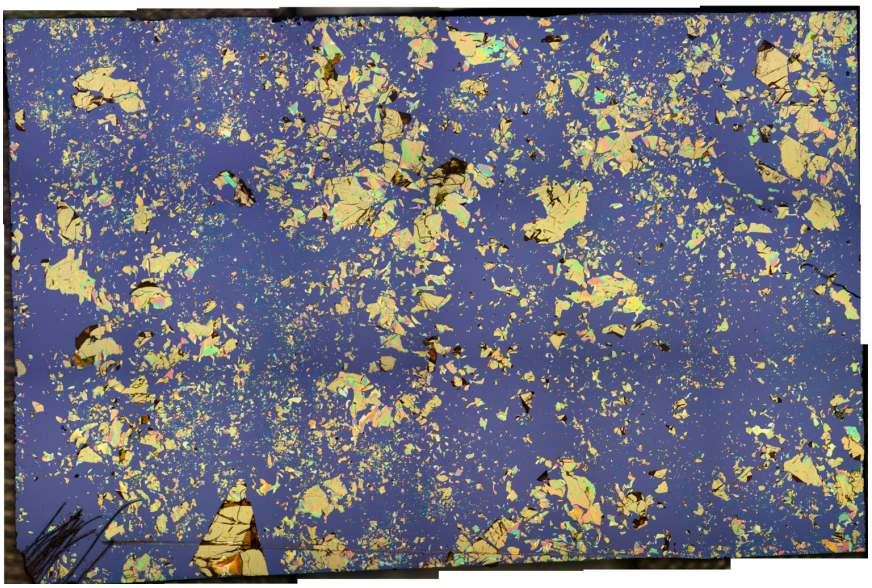

Figure 1.12: Peeled PbI_2 on a Si substrate

Si underneath acts as a partial mirror. Blake et.al. [19] did a thorough analysis of this interference and its consequences for graphene. They created an effective model based on Fresnel's equations; I reproduced this work for GaSe and the code for this can be found in Appendix A.

When using a white light source, the critical question is what will the contrast and color of your samples of interest be. Because our eyes are most sensitive to light in the 500 nm to 600 nm region, this is where it is critical to have high contrast. For graphene, in [19] they concluded that 280 nm or 90 nm oxide thickness provided the best contrast. Fig. 1.13 shows a plot of the contrast for a GaSe monolayer (modeled to be 0.8 nm thick) with the oxide thickness on the horizontal axis and the illuminating wavelength on the vertical axis. Because we use a white light source, as was mentioned above, the important consideration is the contrast near 500 nm to 600 nm, which for our 285 nm oxide thickness wafers provides a fairly good contrast, although an oxide thickness closer to 250 nm or 75 nm would be better.

Also due to the interference's strong dependence on the sample thickness, when viewed with white light, the different sized flakes have different colors. Fig. 1.14 shows

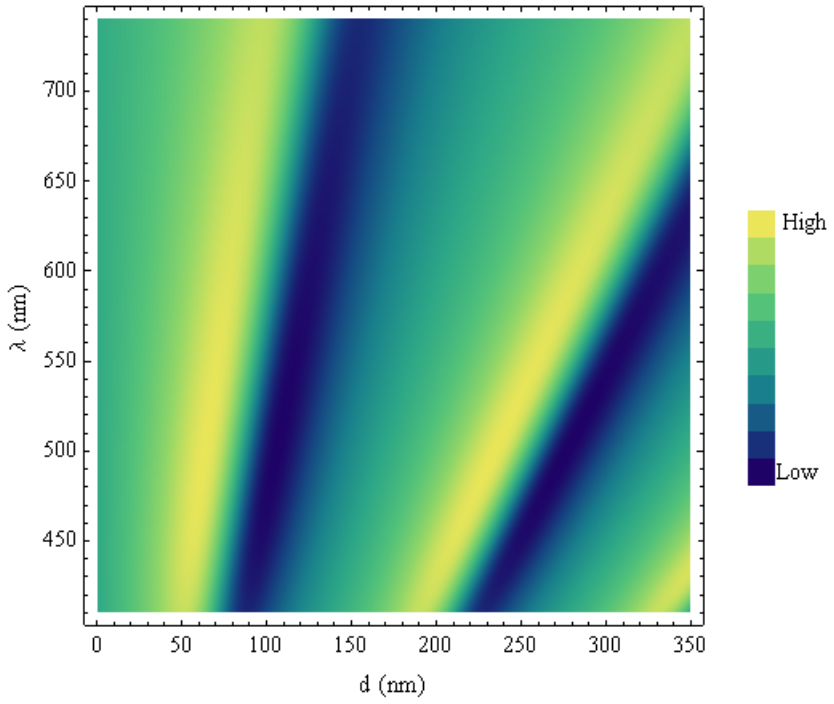

Figure 1.13: Contrast of monolayer of GaSe illuminated with light λ on Si wafer with oxide thickness d

the magnitude of the contrast for various thicknesses of GaSe flakes as a function of wavelength on a Si wafer with oxide thickness 285 nm. This was also calculated using the Fresnel equation approach first developed in [19]. The location of the peaks shifts to the blue for thinner samples; this is consistent with our AFM measurements and is generally consistent with the results for graphene. Note that the color will be somewhat periodic for much thicker samples, thus both the color and the opacity serve as indications of the sample's thickness. This is the primary mechanism which first allowed graphene to be found among the "haystack" of millions of thicker graphite flakes [19] that one produces when making graphene. This is one of the key insights that allowed graphene to first be isolated and studied [1]. Using this same trick, we can easily estimate the thickness of GaSe or PbI_2 flakes simply using optical microscopy. Fig. 1.15 shows a typical sample with a distribution of thicknesses of PbI_2 flakes. Note the wide range of colors present and that dark blue areas near the center are

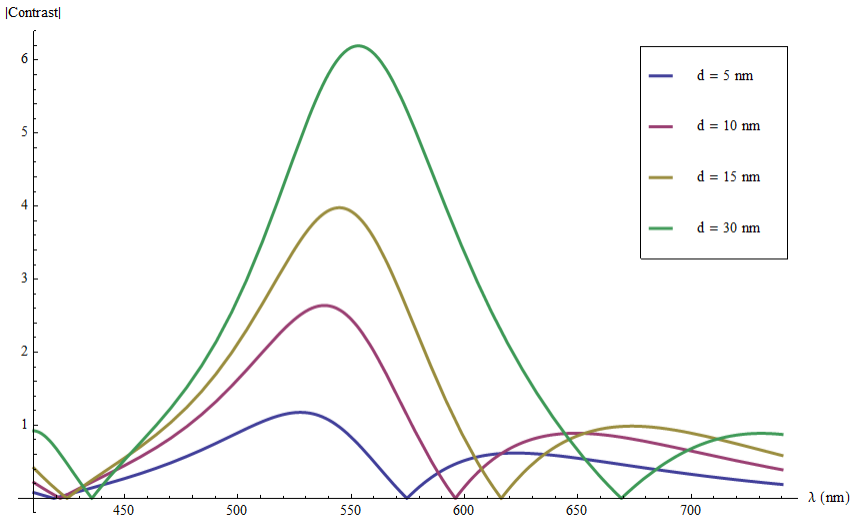

Figure 1.14: Magnitude of the contrast for various thicknesses of GaSe flakes as a function of wavelength λ on Si wafer with oxide thickness 285 nm

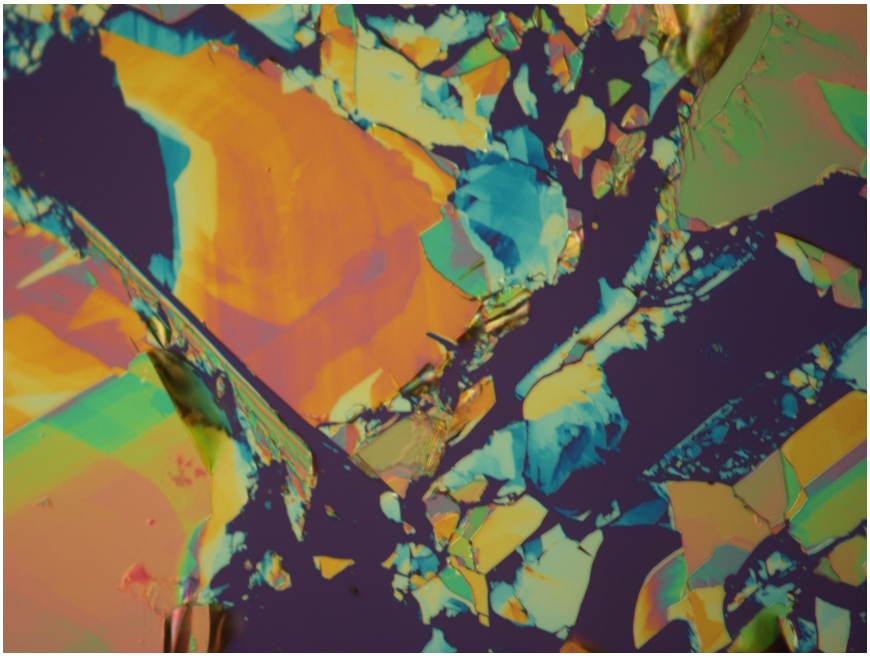

Figure 1.15: A typical sample with a distribution of thickness of PbI_2 flakes on a Si wafer

extremely thin, potentially even monolayers.

1.4 Measurements

In this section I will briefly explain the experiments we performed to measure the excitonic confinement effects in GaSe and PbI_2. The two main experimental efforts that I will focus on is our latest reflection measurement setup and our use of atomic force microscopy (AFM). At the time of writing this, the experiment is not complete, and in addition to simply measuring more data points, we have plans to utilize new tools. With this being said, the experiments and techniques I describe here may not necessarily be the final or most useful ones used by this group, but are the most successful ones used as of now.

1.4.1 Reflection Experiment

Our main optical measurements are conducted using a reflection geometry. These measurements were done on a setup shown in Fig. 1.16. I am particularly proud of the setup that we have built–it has gone through many iterations and contains many custom-built parts. In my opinion the setup is a very clever and effective way to conduct this difficult experiment. In Fig. 1.16 WL stands for white light source, BS stands for beam-splitter, and PMT stands for photomultiplier tube. The ovals are lenses and the mirrors with a curved arrow next to them are flip mirrors. The black line indicates the main optical path. The green line is the optical path we use to image the sample with the measuring light simultaneously incident. The red line indicates the optical path that we use to monitor any fluctuations of the light source and subsequently normalize the signal. I will now carefully explain the setup and its important components.

For our white light source (main path), we use a quartz tungsten halogen lamp, which provides a high quality, relatively smooth blackbody spectrum in the regions

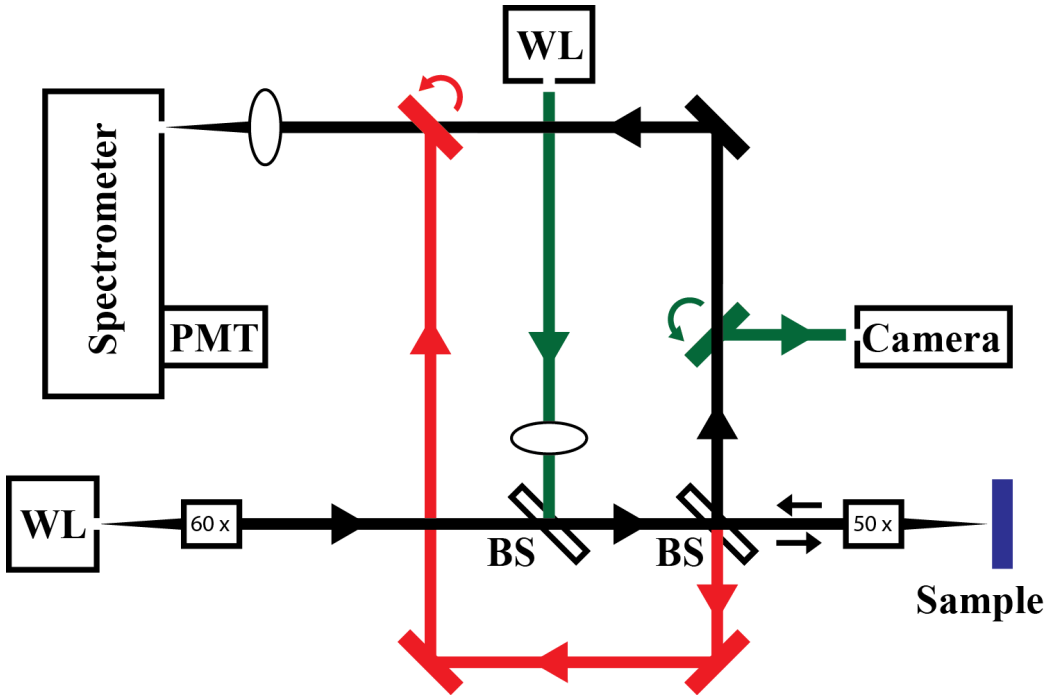

Figure 1.16: A diagram showing our reflection measurement setup.

we are interested in. We then collimate the light using a 50 μm pin hole and a 60x magnification objective lens. After passing through two beam-splitters, whose function will be subsequently explained, the light is focused onto the sample using a 50x magnification objective lens. The sample is held under vacuum at cryogenic temperatures in a cryostat. Currently we are using a cold finger liquid nitrogen (LN_2) reservoir cryostat, but we hope to soon use a cold finger liquid helium (LHe) continuous flow cryostat to reach even lower temperatures. The light then reflects from the sample and is collected back through the 50x objective. After several mirrors, it is focused onto the entrance slit of the spectrometer, a SPEX 1404 double grating monochrometer, which reads the signal using a PMT.

To image the sample, we use the green optical path. Because this white light source is not being measured, we used a much lower quality fiber lamp that is already collimated. Making use of the first beam-splitter, the green path is made colinear with the black path. Also, so that we have a diffuse spot on the sample, we use the

lens before the first beam-splitter in the green optical path to create a diverging beam that is then collimated using the 50x objective. We then image the surface of the sample by using a video camera with a telescope lens, which collects light from the sample by putting the green flip mirror up. If we also turn on the primary white light, thus turning on the black optical path, we can image the sample and see where our beam is focused on the sample. An illustration of this is shown in Fig. 1.17. This is

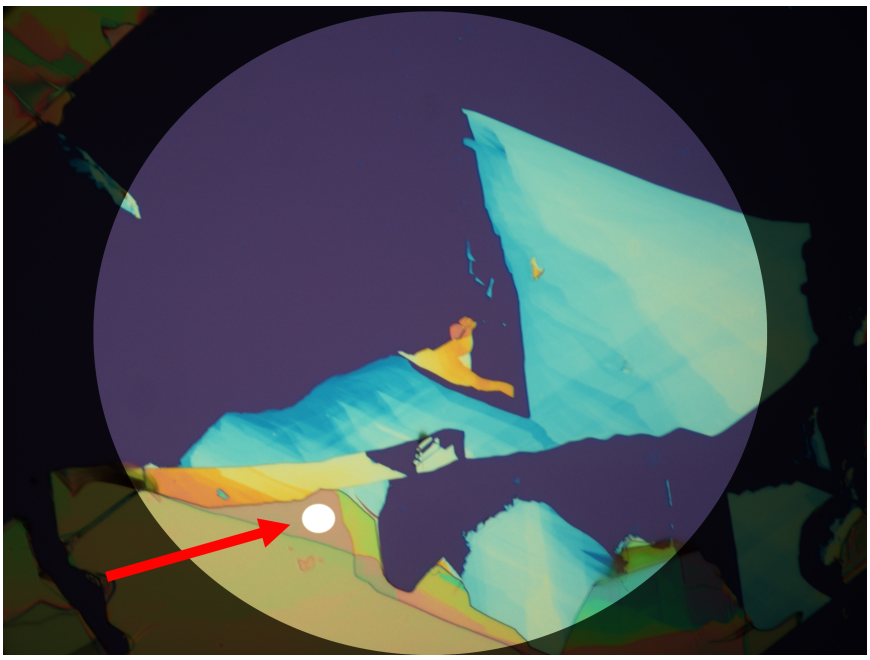

Figure 1.17: An illustration showing what we view in real time using the camera, the red arrow points to the white spot which is the focused measurement beam

an extremely useful technique which allows us to precisely measure very specific areas on the sample. This had previously been quite difficult to achieve due to the very small size of some of the areas. The spot size shown in Fig. 1.17 is approximately 5 μm, which is comparable to our actual spot size.

The red optical path monitors the light source for any fluctuations in power. The light coming from the lamp, which is reflected from the second beam-splitter, is steered to a computer-controlled flip mirror. When the mirror is down, only the black path enters the spectrometer. When the mirror is up, the red path enters the spectrometer

and the back of the mirror blocks the black path. Thus, we are measuring the light directly from the lamp OR the light coming from the sample.

Our pre-measurement procedure is roughly as follows. We first identify which areas we would like to measure using a microscope and then cool the sample in the cryostat. Once the sample and the cryostat have reached thermal equilibrium and have stopped contracting, we image the sample using the camera and move things so that the beam is on the area of interest. To actually take data, we employ the following scheme. We first measure the sample, I will call this signal I_1. Then we measure a reference, call it I_2, which is accomplished by placing a small mirror next to the sample in the cryostat.

Each of these measurements takes a significant amount of time–we need to measure the signal for each point in the spectrum, and integrate long enough at each point to achieve a good signal to noise ratio; a typical spectrum will take about one hour. We had previously made some measurements that indicated that the spectrum of the lamp changed slightly on this time scale. Therefore, we could not be confident that our reference was truly a reference, and also the beginning and end of a spectrum could have noticeable differences due only to these changes. In order to correct for this, we implemented the monitor (red path) which measures the light coming directly from the lamp after taking each data point. We do this during both the sample and the reference measurements, I will call those signals I_{1m} and I_{2m} respectively. Therefore, the normalized signals I_{jn} are

$$I_{1n} = \frac{I_1}{I_{1m}} \qquad I_{2n} = \frac{I_2}{I_{2m}} \tag{1.6}$$

Dividing I_{1n} by I_{2n} gives the reflection data of the sample

$$I = \frac{I_{1n}}{I_{2n}} = \frac{I_1}{I_{1m}}\frac{I_{2m}}{I_2} = \frac{I_1}{I_2}\frac{I_{2m}}{I_{1m}} \tag{1.7}$$

This is the signal that we are ultimately analyzing and it is what is being shown in all of the PbI_2 spectra in Section 1.5.

1.4.2 Atomic force microscopy

After measuring the samples optically, we then measure them using AFM. The primary purpose of this measurement is to determine how thick the measured sample was. This helps enormously with fitting the reflectivity measurement to our model, because as was indicated previously, the optical spectrum is very sensitive to the thickness of the sample. The secondary purpose of taking AFM measurments is so that we may verify how uniform the thickness was in the area we measured. Obviously we can observe large changes in thickness using the microscope or the camera in our setup, however small changes can be very difficult to see and this technique cleary provides that information. All of the AFM measurements were performed at the University of Michigan Electron Microbeam Analysis Laboratory (EMAL), using a Veeco Dimension Icon Atomic Force Microscope. The tips we used are MikroMasch SPM probe tips with a tip radius of less than 10 nm.

The basic idea of how AFM works is that a cantilever, which has an atomically sharp tip on the bottom, is tapped against the surface of a sample to obtain very precise information about the sample's surface. By scanning across the edge of our samples, we can directly measure the sample's thickness. Although this is fairly simple to understand, and by using a fully packaged commercial system, is fairly simple to use, there can be some very complicated issues that arise when measuring very thin samples [20]. One can understand an example of this by considering exactly what we are measuring when we measure the sample's thickness. We are measuring the height difference from the top of the oxide layer to the top of the sample. Therefore, if for any reason the sample is not in perfect contact with the top of the oxide layer, we will overestimate the thickness. Another question we have is regarding whether the

cantilever tip actually touches either surface, and if it doesn't, does it come equally close to both? We have not tried to look into these issues extensively, only to be aware of them, and to proceed very carefully with the AFM measurements.

A typical AFM scan is shown next to an optical image of the same sample in Fig. 1.18. Notice how the AFM scan provides a much more detailed image of the surface

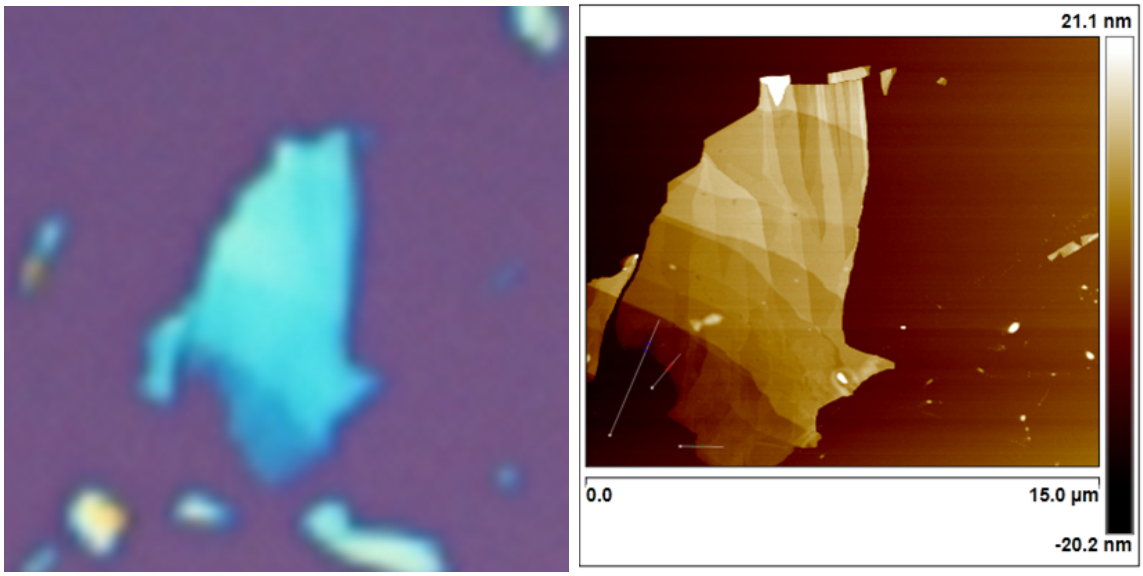

Figure 1.18: (Left) an optical image of a GaSe flake (Right) An AFM scan of the same sample

of the sample, features that could never be resolved using diffraction limited optical imaging. Also observe how the AFM scan reveals that parts of the sample which appeared to have a uniform thickness actually do not. This particular sample is quite thin, the dark blue region in the optical image (lower left corner of the sample) is approximately 13 nm.

1.5 Results and Interpretation

I will now present some of our most compelling data on PbI_2 and then give a brief interpretation of these results. I will not present our data for GaSe because the exciton is easier to see in PbI_2 and all of our most recent efforts have been focused

exclusively on PbI_2. As I have mentioned previously, this data is not necessarily our final data, it is only our best results thus far. With that being said, we do trust this data and believe in its veracity, we simply want to try other experiments and probes as well.

I would like to first explain some of the large scale features of the data. As was explained before, the sample and oxide layer creates a Fabry-Perot type of interference which is highly dependent on the sample's thickness–recall that this is the mechanism for the dramatic color changes observed in the thin samples. Spectrally, this creates

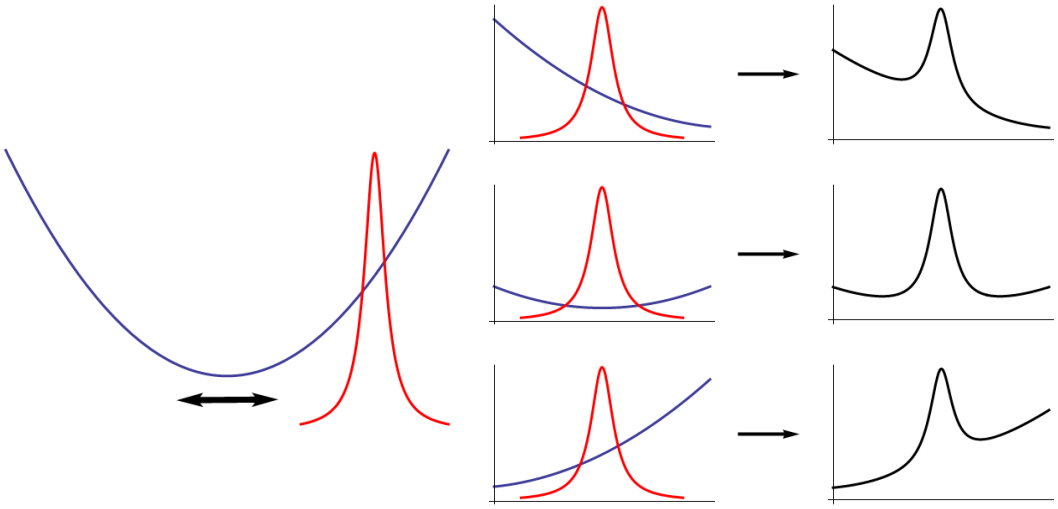

Figure 1.19: Adding a Lorentzian and a parabola can produce very different looking backgrounds

complex looking backgrounds for our data. The interference produces a sinusoidal-like shape where the local period is dependent on the thickness. For very thin samples, the frequency approachs zero, thus producing a flat background. As the frequency, changes the background may have very different shapes in the region we are interested in. Fig. 1.19 demonstrates this by adding a Lorentzian to a parabola at different relative locations. The Lorentzian is meant to represent the exciton. The parabola represents the background, while although not sinusoidal for many of spectra shown below, the background is approximately parabolic.

When looking at the data, keep the background changes in mind, it is not very interesting and in fact only makes our data analysis more difficult. What is interesting to observe is the location of the exciton peak, whether there are additional peaks, or other interesting changes that may occur very close to the exciton resonance, which for PbI_2 occurs near 497 nm. All of the data shown in this section are taken at 77 K. As a reference, Fig. 1.20 shows the reflection spectrum of a bulk piece of PbI_2. The

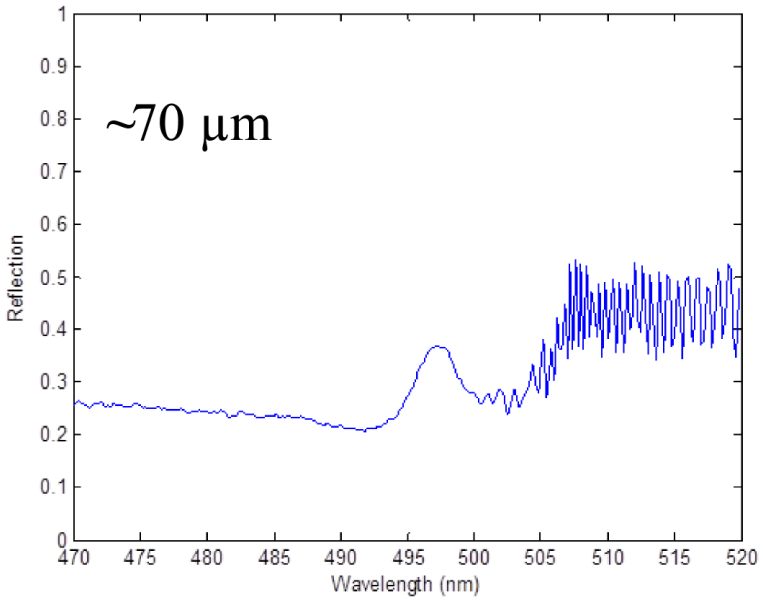

Figure 1.20: Reflection spectrum of a bulk ($\sim$ 70 μm) piece of PbI_2

sample is bulk in the sense that there won't be any quantum confinement effects, but the very fast oscillations below the gap indicate that the sample is thin enough to observe Fabry-Perot interference. The peak around 497 nm is the exciton.

Fig. 1.21 shows spectra for several very thin PbI_2 flakes. Looking past the background changes, it appears that the exciton peak is indeed moving to higher energies (lower wavelengths) as we predicted based off of the analysis of a simple square potential well. Higher order excitons may also be visible, but it is difficult to tell because, if they are present they are on the order of the noise. Most importantly Fig. 1.22 shows the reflection spectrum of a 14 nm thick sample–this is one of the thinnest

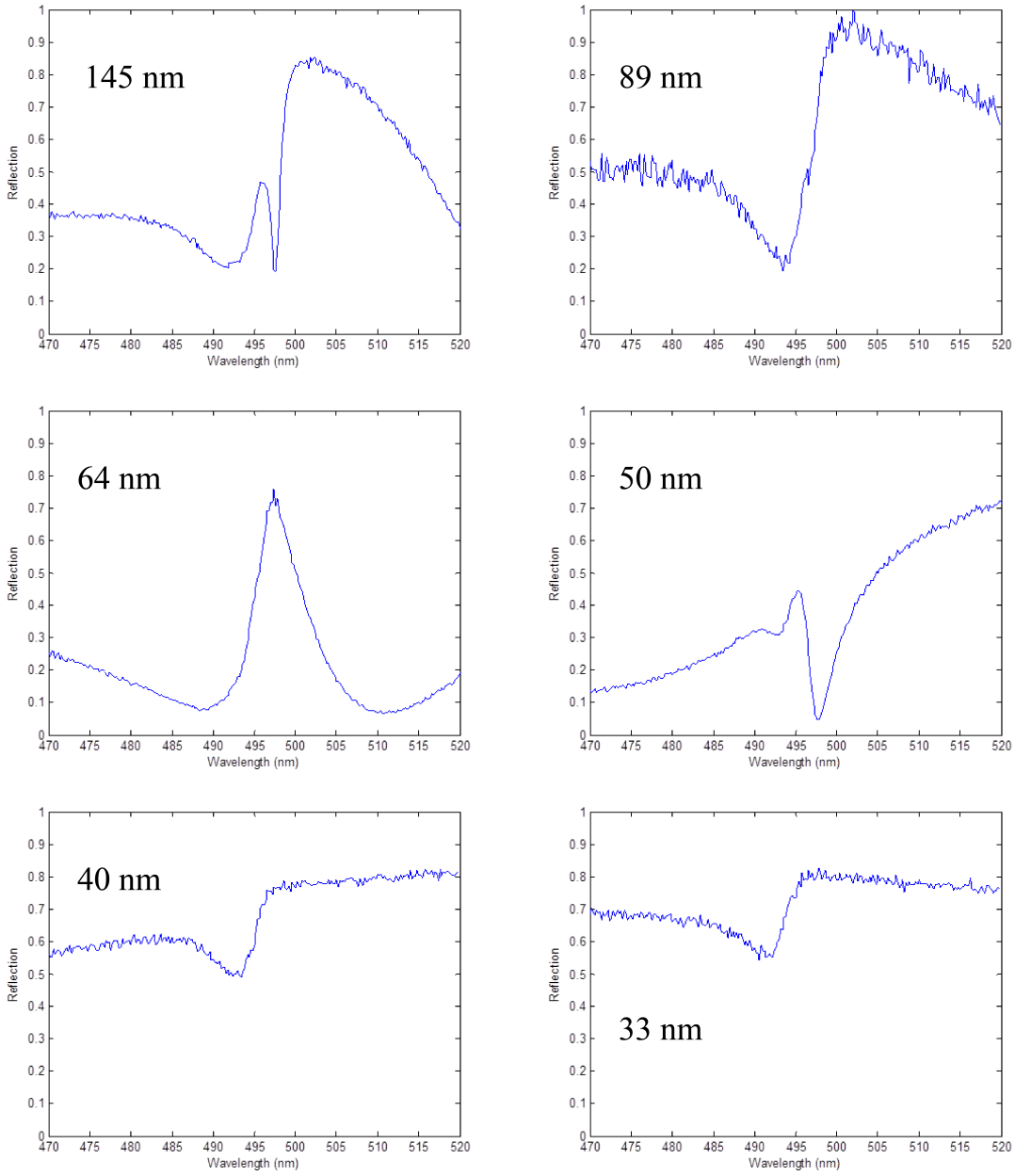

Figure 1.21: Reflection spectra of very thin PbI_2 flakes, the thickness of the sample is indicated on the plot

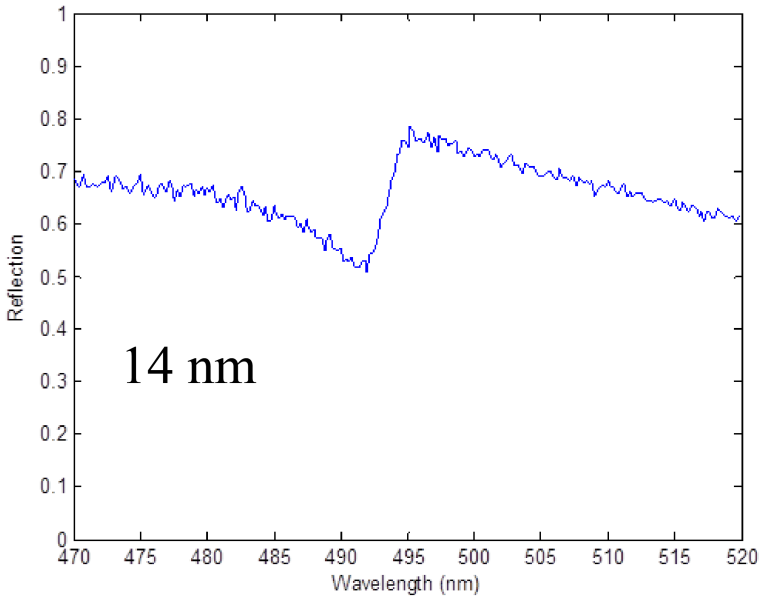

Figure 1.22: Reflection spectra of a 14 nm thick PbI_2 flake, one of the thinest we have measured.

samples we have measured.

1.6 Conclusions and Further Work

I have described our experiment studying exciton confinement in atomically thin PbI_2 and GaSe nanosheets. We have demonstrated that using the techniques employed in the discovery of graphene we can isolate and study these natural quantum wells. I have also given some theoretical background to help understand the experiment and our results. I briefly explained our motivation for conducting this experiment. The experimental results agree very generally with the simplistic model explained. The exciton does appear to shift to higher energies and there could possibly be higher order excitons appearing.

This experiment is not over yet, we are constantly improving the experimental setup and gaining a better understanding of the sources of error present. Furthermore,

we hope to soon measure at LHe temperatures to be able to better resolve the exciton. We are striving to better understand the AFM measurements and control for any errors introduced there. The present results provide strong evidence that there is interesting physics occuring, but we hope to be able to observe and understand them better in the future.

We are also working very hard to develop a model to explain our data that would allow us to completely understand the physics occuring. Our theoretical efforts thus far have been focused on using reduced dimensionality models for excitons to try and fit our data to extract the material's permitivity as a function of thickness. However these fits are not completely adequate, and we are suspicious that we need to include other effects as well, possibly including polaritons, and potentially the additional boundary condition problem.

I believe that these natural quantum wells are a fundamentally new way to study exciton confinement, and as such, have the potential to expose new and interesting physics. Furthermore, as was demonstrated by graphene, these nanomaterials can have remarkable properties, many of which nobody had ever predicted. To my knowledge, we are the first to isolate and study atomically thin GaSe and PbI_2. There is a plethora of new questions to be asked and many things to learn from these new materials systems. I hope that our experiment and those to follow will be able to advance our current understanding of excitons and ultimately give us a deeper understanding of physics.

CHAPTER II

Numerical and Analytical Analysis of Subwavelength Focusing Using a Negative Refractive Index Slab

In recent years there has been considerable interest and much effort [21–23] put into the study of materials possesing a negative refractive index, henceforth referred to as a left-handed material (LHM). In 2000 Pendry [24] showed that an impedence matched slab of LHM, which Veselgo [25] had shown earlier to act as a lens, could perserve the near-field components of an image and hence behave as a perfect lens. There has since been a deluge of work along with some controversy in analyzing the use of a LHM to achieve super-resolution [26] – [47]. In this chapter we analyze the transmitted fields through a LHM that posseses slight deviations from impedence matching. Section 2.2 is dedicated to numerically analyzing the transmitted fields from a point dipole source. In section 2.3 we carefully develop an analytical expression for the transmitted fields from a line of dipole sources, where we expand on the results first published by Merlin [26] in 2004 while detailing their derivation.

2.1 Geometry

We first set up the general problem with the geometry as is shown in Fig. 2.1. The

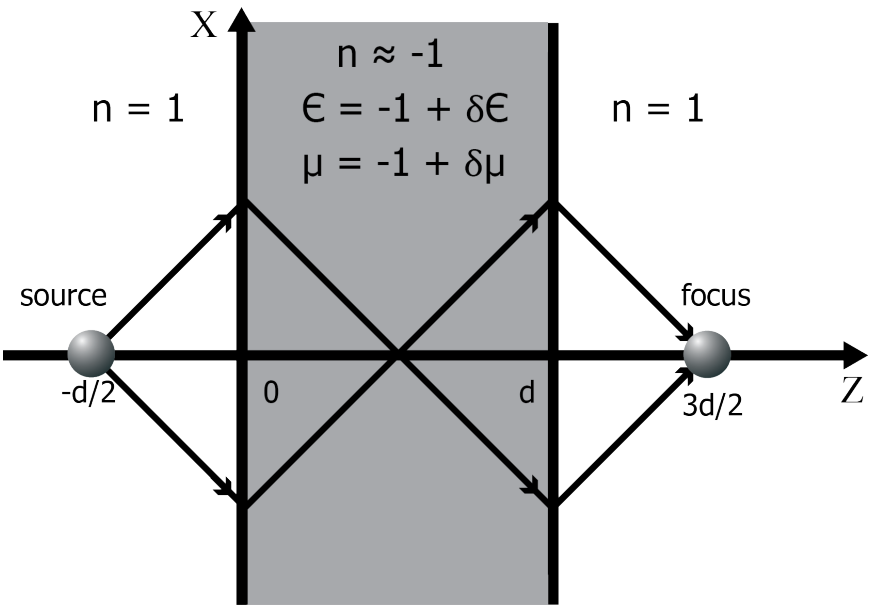

Figure 2.1: The geometry being considered, where the region $0 \leq z \leq d$ is occupied by a left-handed material with permitivity and permeability $\epsilon = -1+\delta\epsilon$ and $\mu = -1+\delta\mu$. The regions $z < 0$ and $z > d$ are vacuum.

region $0 \leq z \leq d$ is occupied by a left-handed material with permitivity $\epsilon = -1 + \delta\epsilon$ and permeability $\mu = -1 + \delta\mu$, such that $\delta\epsilon = \delta\epsilon_1 + i\delta\epsilon_2 = |\delta\epsilon|e^{i\phi_0}$ is a small complex number with $|\delta\epsilon| \ll 1$ and $\delta\epsilon_2 > 0$, i.e. $0 < \phi_0 < \pi$, and with $\delta\mu$ is defined analogously. The regions $z < 0$ and $z > d$ are vacuum. Our goal is to find the magnetic H-field in the region $z > d$.

2.2 Point Dipole Source

2.2.1 Source Field

On the z axis at $z = -d/2$ we place an electric dipole with current $\mathbf{j} = P_0\delta(x)\delta(y)\delta(z+d/2)e^{-i\omega t}\hat{\mathbf{n}}$. Without loss of generality, the polarization can be taken to oscillate in the xz plane. There is a focal plane inside the slab at $z = d/2$ and the focal plane outside of the slab is at $z = 3d/2$. Making use of the Weyl decomposition, the Hertz

pontential of this dipole [48] is given by

$$\mathbf{\Pi}_e = e^{-i\omega t}(P_0/2\pi)\hat{\mathbf{n}} \int_{-\infty}^{+\infty} e^{i(q_x x + q_y y)} e^{-\kappa_0 |z+d/2|} \frac{dq_x dq_y}{\kappa_0} \tag{2.1}$$

where

$$\kappa = \begin{cases} -i\sqrt{\epsilon\mu\omega^2/c^2 - q^2} & \text{for } q^2 \leq \epsilon\mu\omega^2/c^2 \\ \sqrt{q^2 - \epsilon\mu\omega^2/c^2} & \text{for } q^2 \geq \epsilon\mu\omega^2/c^2 \end{cases} \tag{2.2}$$

$$q^2 = q_x^2 + q_y^2 \qquad \kappa_0 = \kappa \text{ for } \epsilon = \mu = -1 \tag{2.3}$$

Recall that by definition of the Hetz potential [48] $\mathbf{H}_{source} = \frac{1}{c}\nabla \times \frac{\partial}{\partial t}\mathbf{\Pi}_e$, noting that $\frac{\partial}{\partial t}\mathbf{\Pi}_e = -i\omega\mathbf{\Pi}_e \;\; \Rightarrow \;\; \mathbf{H}_s = \frac{-i\omega}{c}\nabla \times \mathbf{\Pi}_e$. Recall that we took the dipole to oscillate in the xz plane and thus $\hat{\mathbf{n}} = n_x\hat{\mathbf{x}} + n_z\hat{\mathbf{z}}$. Also note that because $|z| \leq d/2$ we can write the exponent argument $|z + d/2|$ as $(z + d/2)$. Taking the curl yields

$$\nabla \times \mathbf{\Pi}_e = [in_z q_y \hat{\mathbf{x}} - (n_x\kappa_0 + in_z q_x)\hat{\mathbf{y}} - in_x q_y \hat{\mathbf{z}}]\mathbf{\Pi}_e \tag{2.4}$$

Defining $\mathbf{v}(q_x, q_y) \equiv in_z q_y \hat{\mathbf{x}} - (n_x\kappa_0 + in_z q_x)\hat{\mathbf{y}} - in_x q_y \hat{\mathbf{z}}$, we see that

$$\mathbf{H}_s = -i\omega e^{-i\omega t}(P_0/2\pi) \int_{-\infty}^{+\infty} e^{i(q_x x + q_y y)} e^{-\kappa_0(z+d/2)} \mathbf{v}(q_x, q_y) \frac{dq_x dq_y}{\kappa_0} \tag{2.5}$$

Henceforth we shall ignore the time dependence of the fields (or equivalently consider them at $t = 0$). Defining $\alpha \equiv \frac{-i\omega P_0}{2\pi\kappa_0}$ and $\Psi \equiv e^{i(q_x x + q_y y)} e^{-\kappa_0(z+d/2)}$, we can write the source magnetic field as

$$\mathbf{H}_s = \int_{-\infty}^{+\infty} \Psi\alpha\mathbf{v}(q_x, q_y) dq_x dq_y \tag{2.6}$$

2.2.2 Transverse Decomposition of Source Field

We decompose the source wave into the sum of two plane waves, one with its electric field polarized parallel to the slab and one with its magnetic field polarized parallel to the slab, that is we let $\mathbf{H}_s = \mathbf{H}^{TM} + \mathbf{H}^{TE}$. Note that from Fraday's Law $\nabla \times \mathbf{E} = -\frac{1}{c}\frac{\partial \mathbf{B}}{\partial t}$ in vacuum where $\mathbf{B} = \mathbf{H}$, noting that $\frac{\partial \mathbf{H}}{\partial t} = -i\omega\mathbf{H}$ we see that $\mathbf{H}^{TE} = -\frac{ic}{\omega}\nabla \times \mathbf{E}^{TE}$. We now rotate in the xy plane by the angle ϕ to (x', y') coordinates by using the rotation matrix such that

$$\begin{pmatrix} x' \\ y' \end{pmatrix} = \begin{pmatrix} \cos\phi & \sin\phi \\ -\sin\phi & \cos\phi \end{pmatrix} \begin{pmatrix} x \\ y \end{pmatrix} \tag{2.7}$$

By defining $q_x \equiv q\cos\phi$ and $q_y \equiv q\sin\phi$ we see that $qx' = q_x x + q_y y$ and $qy' = -q_y x + q_x y$. We now define

$$\begin{aligned} \mathbf{H}^{TM} &= \int_{-\infty}^{+\infty} h_0 \hat{\mathbf{y}}' \Psi dq_x dq_y \\ \mathbf{E}^{TE} &= \int_{-\infty}^{+\infty} e_0 \hat{\mathbf{y}}' \Psi dq_x dq_y \end{aligned} \tag{2.8}$$

Using $\mathbf{H}^{TE} = -\frac{ic}{\omega}\nabla \times \mathbf{E}^{TE}$ we see that

$$\mathbf{H}^{TE} = \int_{-\infty}^{+\infty} e_0 \frac{c}{\omega}(-i\kappa_0 \hat{\mathbf{x}}' + q\hat{\mathbf{z}})\Psi dq_x dq_y \tag{2.9}$$

Applying the coordinate rotation to $\mathbf{v}(q_x, q_y) \;\Rightarrow\; \mathbf{v}(q_x, q_y) \rightarrow \mathbf{v}(q, \phi)$

$$\begin{aligned}
\mathbf{v}(q,\phi) &= in_z q\sin\phi\hat{\mathbf{x}} - (n_x\kappa_0 + in_z q\cos\phi)\hat{\mathbf{y}} - in_x q\sin\phi\hat{\mathbf{z}} \\
&= in_z q(\sin\phi\hat{\mathbf{x}} - \cos\phi\hat{\mathbf{y}}) - n_x\kappa_0\hat{\mathbf{y}} - in_x q\sin\phi\hat{\mathbf{z}} \\
&= -in_z q\hat{\mathbf{y}}' - n_x\kappa_0(\sin\phi\hat{\mathbf{x}}' + \cos\phi\hat{\mathbf{y}}') - in_x q\sin\phi\hat{\mathbf{z}} \\
&= -n_x\kappa_0\sin\phi\hat{\mathbf{x}}' - (in_z q + n_x\kappa_0\cos\phi)\hat{\mathbf{y}}' - in_x q\sin\phi\hat{\mathbf{z}} \qquad (2.10)
\end{aligned}$$

Recalling that $\mathbf{H}_s = \mathbf{H}^{TM} + \mathbf{H}^{TE}$ and inspecting eqns: (2.6), (2.8), (2.9), and (2.10) we see that $\mathrm{H}_{s,x'} = \mathrm{H}^{TE}_{x'}$

$$\int_{-\infty}^{+\infty} \Psi\alpha(-n_x\kappa_0\sin\phi)dq_x dq_y = \int_{-\infty}^{+\infty} e_0\frac{c}{\omega}(-i\kappa_0)\Psi dq_x dq_y$$

Solving for e_0 yields

$$e_0 = -\frac{i\omega}{c}\alpha n_x\sin\phi \qquad (2.11)$$

Similarly we see that $\mathrm{H}_{s,y'} = \mathrm{H}^{TE}_{y'}$

$$\int_{-\infty}^{+\infty} \Psi\alpha(-in_z q - n_x\kappa_0\cos\phi)dq_x dq_y = \int_{-\infty}^{+\infty} h_0\Psi dq_x dq_y$$

Solving for h_0 yields

$$h_0 = -\alpha(in_z q + n_x\kappa_0\cos\phi) \qquad (2.12)$$

2.2.3 Derivation of Transmission Functions

We now derive the transmission functions T_M and T_E for the transverse fields across the slab, therefore we define the following regions: I, II, III as $z < 0, 0 < z < d$,

and $z > d$ respectivley with the field defined there as

$$\mathrm{E}_{y'} = \begin{cases} \mathrm{E}_0 e^{iqx'} e^{-\kappa_0(z+d/2)} + \mathrm{E}_\mathrm{R} e^{iqx'} e^{+\kappa_0(z+d/2)} & \mathrm{I} \\ \mathrm{E}_- e^{iqx'-\kappa z} + \mathrm{E}_+ e^{iqx'+\kappa z} & \mathrm{II} \\ \mathrm{E}_\mathrm{T} e^{iqx'-\kappa_0 z} & \mathrm{III} \end{cases} \tag{2.13}$$

With $\mathbf{H}$ defined analogously. We therefore define $T_E \equiv \frac{\mathrm{E_T}}{\mathrm{E_0}}$ and $T_M \equiv \frac{\mathrm{H_T}}{\mathrm{H_0}}$. We have the following boundary conditions: $\mathrm{E}_{y'}$ is continuous, and from Faraday's Law $\nabla \times \mathbf{E} = -\frac{i\omega\mu}{c}\mathbf{H}$ we see that $\frac{1}{\mu}\frac{\partial E_{y'}}{\partial z}$ must be continuous. Note that we are in Gaussian units, and thus in vacuum $\mu = \mu_0 = 1$.

B.C.'s at $z = 0$

$$\begin{aligned} \mathrm{E}_0 e^{-\kappa_0 d/2} + \mathrm{E}_\mathrm{R} e^{+\kappa_0 d/2} &= \mathrm{E}_- + \mathrm{E}_+ \\ \kappa_0(-\mathrm{E}_0 e^{-\kappa_0 d/2} + \mathrm{E}_\mathrm{R} e^{+\kappa_0 d/2}) &= \tfrac{\kappa}{\mu}(-\mathrm{E}_- + \mathrm{E}_+) \end{aligned} \tag{2.14}$$

B.C.'s at $z = d$

$$\begin{aligned} \mathrm{E}_- e^{-\kappa d} + \mathrm{E}_+ e^{+\kappa d} &= \mathrm{E}_\mathrm{T} e^{-\kappa_0 d} \\ \tfrac{\kappa}{\mu}(-\mathrm{E}_- e^{-\kappa d} + \mathrm{E}_+ e^{+\kappa d}) &= -\kappa_0 \mathrm{E}_\mathrm{T} e^{-\kappa_0 d} \end{aligned} \tag{2.15}$$

Isolating E_+ & E_- using (2.15) gives

$$\begin{aligned} 2\mathrm{E}_+ &= \mathrm{E}_\mathrm{T} e^{-(\kappa_0+\kappa)d}(1 - \mu\tfrac{\kappa_0}{\kappa}) \\ 2\mathrm{E}_- &= \mathrm{E}_\mathrm{T} e^{-(\kappa_0-\kappa)d}(1 + \mu\tfrac{\kappa_0}{\kappa}) \end{aligned} \tag{2.16}$$

Isolating E_0 using (2.14) gives

$$2\mathrm{E}_0 e^{-\kappa_0 d/2} = \mathrm{E}_-(1 + \frac{1}{\mu}\frac{\kappa}{\kappa_0}) + \mathrm{E}_+(1 - \frac{1}{\mu}\frac{\kappa}{\kappa_0})$$

$$= \frac{1}{2}\mathrm{E}_\mathrm{T} e^{-(\kappa_0-\kappa)d}(1 + \mu\frac{\kappa_0}{\kappa})(1 + \frac{1}{\mu}\frac{\kappa}{\kappa_0}) + \frac{1}{2}\mathrm{E}_\mathrm{T} e^{-(\kappa_0+\kappa)d}(1 - \mu\frac{\kappa_0}{\kappa})(1 - \frac{1}{\mu}\frac{\kappa}{\kappa_0}) \Rightarrow$$

$$\mathrm{E}_0 = \frac{1}{4}\mathrm{E}_\mathrm{T} e^{+\kappa d - \kappa_0 d/2}\frac{(\kappa + \mu\kappa_0)^2}{\mu\kappa\kappa_0} - \frac{1}{4}\mathrm{E}_\mathrm{T} e^{-\kappa d - \kappa_0 d/2}\frac{(\kappa - \mu\kappa_0)^2}{\mu\kappa\kappa_0} \Rightarrow$$

$$T_E \equiv \frac{\mathrm{E_T}}{\mathrm{E_0}} = \frac{4\kappa\kappa_0\mu e^{\kappa_0 d/2}}{(\kappa+\mu\kappa_0)^2 e^{\kappa d} - (\kappa-\mu\kappa_0)^2 e^{-\kappa d}} \tag{2.17}$$

Note that from Ampere's Law $\nabla \times \mathbf{H} = \frac{4\pi}{c}\mathbf{J}_f + \frac{1}{c}\frac{\partial}{\partial t}\mathbf{D}$ with $\mathbf{J}_f = 0, \mathbf{D} = \epsilon\mathbf{E}$ and $\frac{\partial}{\partial t}\mathbf{E} = -i\omega\mathbf{E} \Rightarrow \nabla \times \mathbf{H} = -\frac{i\omega\epsilon}{c}\mathbf{E}$, which is analogous to Faraday's Law with μ replaced with ϵ, and we see that the boundary conditions on $\mathbf{H}$ are analogous to those used above on $\mathbf{E}$, therefore we can simply replace μ in T_E with ϵ to get

$$T_M \equiv \frac{\mathrm{H_T}}{\mathrm{H_0}} = \frac{4\kappa\kappa_0\epsilon e^{\kappa_0 d/2}}{(\kappa+\epsilon\kappa_0)^2 e^{\kappa d} - (\kappa-\epsilon\kappa_0)^2 e^{-\kappa d}} \tag{2.18}$$

2.2.4 Construction of the Transmitted Field

Combining (2.6) & (2.10) and breaking into vector components yields

$$\begin{aligned}
\mathrm{H}_{s,x'} &= -\int_{-\infty}^{+\infty} \alpha n_x \kappa_0 \sin\phi \Psi dq_x dq_y \\
\mathrm{H}_{s,y'} &= -\int_{-\infty}^{+\infty} \alpha(in_z q + n_x\kappa_0\cos\phi)\Psi dq_x dq_y \\
\mathrm{H}_{s,z} &= -\int_{-\infty}^{+\infty} \alpha i n_x q \sin\phi \Psi dq_x dq_y
\end{aligned} \tag{2.19}$$

We now rotate back to xy coordinates using (2.7) in reverse

$$\begin{pmatrix} x \\ y \end{pmatrix} = \begin{pmatrix} \cos\phi & -\sin\phi \\ \sin\phi & \cos\phi \end{pmatrix} \begin{pmatrix} x' \\ y' \end{pmatrix} \tag{2.20}$$

Recalling that $\mathbf{H}_s = \mathbf{H}_s^{TM} + \mathbf{H}_s^{TE} \Rightarrow \mathbf{H}_t = T_M\mathbf{H}_s^{TM} + T_E\mathbf{H}_s^{TE}$ and by inspecting (2.8) & (2.9) we see that $\mathbf{H}_s^{TM}$ and $\mathbf{H}_s^{TE}$ exist only in $\hat{\mathbf{x}}'$ and $\hat{\mathbf{z}}'$ respectivley, therefore

the transmitted field is

$$\begin{pmatrix} \mathrm{H}_{t,x} \\ \mathrm{H}_{t,y} \\ \mathrm{H}_{t,z} \end{pmatrix} = \begin{pmatrix} \cos\phi & -\sin\phi & 0 \\ \sin\phi & \cos\phi & 0 \\ 0 & 0 & 1 \end{pmatrix} \begin{pmatrix} T_E \mathrm{H}_{s,x'} \\ T_M \mathrm{H}_{s,y'} \\ T_E \mathrm{H}_{s,z} \end{pmatrix} \tag{2.21}$$

Carrying out the multiplication, and noting that T_M & T_E were defined assuming the transmitted fields $\propto e^{-\kappa_0 z}$ and $\not\propto e^{-\kappa_0(z+d/2)}$ as is in Ψ, yields

$$\mathrm{H}_{t,x} = \int_{-\infty}^{+\infty} \alpha e^{i(q_x x + q_y y)} e^{-\kappa_0 z} \left(-n_x \kappa_0 \sin\phi T_E \cos\phi + \left(i n_z q + n_x \kappa_0 \cos\phi\right) T_M \sin\phi\right) dq_x dq_y$$

$$\mathrm{H}_{t,y} = \int_{-\infty}^{+\infty} \alpha e^{i(q_x x + q_y y)} e^{-\kappa_0 z} \left(-n_x \kappa_0 \sin\phi T_E \sin\phi - \left(i n_z q + n_x \kappa_0 \cos\phi\right) T_M \cos\phi\right) dq_x dq_y$$

$$\mathrm{H}_{t,z} = \int_{-\infty}^{+\infty} \alpha e^{i(q_x x + q_y y)} e^{-\kappa_0 z} \left(-i n_x q \sin\phi T_E\right) dq_x dq_y$$

We now transform by recalling that $q_x = q\cos\phi$ & $q_y = q\sin\phi, \Rightarrow dq_x dq_y \to q dq d\phi$. Note that $q^2 = q_x^2 + q_y^2 \Rightarrow q \geq 0$ and thus we change our integration limits. We also transform the geometric variables by letting $x = r\cos\psi$ & $y = r\sin\psi \Rightarrow q_x x + q_y y = qr(\cos\phi\cos\psi + \sin\phi\sin\psi) = qr\cos(\phi - \psi)$, therefore

$$\mathrm{H}_{t,x} = \int_0^{\infty} \alpha e^{iqr\cos(\phi-\psi)} e^{-\kappa_0 z} [n_x \kappa_0 \sin\phi\cos\phi(T_M - T_E) + i n_z q \sin\phi T_M] q dq d\phi \tag{2.22}$$

$$\mathrm{H}_{t,y} = \int_0^{\infty} \alpha e^{iqr\cos(\phi-\psi)} e^{-\kappa_0 z} [-n_x \kappa_0 (\sin^2\phi T_E + \cos^2\phi T_M) - i n_z q \cos\phi T_M] q dq d\phi \tag{2.23}$$

$$\mathrm{H}_{t,z} = \int_0^{\infty} \alpha e^{iqr\cos(\phi-\psi)} e^{-\kappa_0 z} [-i n_x q \sin\phi T_E] q dq d\phi \tag{2.24}$$

We now do a variable substitution and define $\theta \equiv \phi - \psi$, i.e. $e^{iqr\cos(\phi-\psi)} \rightarrow e^{iqr\cos\theta}$, and noting that ψ is a geometric variable $\Rightarrow d\phi \rightarrow d\theta$ also note that $\phi = \theta + \psi \Rightarrow \sin\phi = \sin\theta\cos\psi + \cos\theta\sin\psi$ & $\cos\phi = \cos\theta\cos\psi - \sin\theta\sin\psi$. Under this variable subsitution and considering only the angular part of (2.22)

$$\mathrm{H}_{t,x}(\theta) = \int_0^{2\pi} e^{iqrcos\theta}[n_x\kappa_0(\sin\theta\cos\psi + \cos\theta\sin\psi)(\cos\theta\cos\psi - \sin\theta\sin\psi) \bullet(T_M - T_E) + iqn_z(\sin\theta\cos\psi + \cos\theta\sin\psi)T_M]d\theta$$

Simplifying the trig and using (B.2) & (B.4), found in appendix B, yields

$$\mathrm{H}_{t,x}(\theta) = -2\pi n_z q\sin\psi T_M J_1(qr) + \frac{1}{2}\int_0^{2\pi} e^{iqrcos\theta} n_x\kappa_0[\cos(2\psi)\sin(2\theta) + \cos(2\theta)\sin(2\psi)](T_M - T_E)d\theta$$

Simplifying using (B.3) & (B.5), and combining with the rest of (2.22) we obtain

$$\boxed{\mathrm{H}_{t,x} = \int_0^{\infty} -\pi\alpha q e^{-\kappa_0 z}[n_x\kappa_0\sin(2\psi)J_2(qr)(T_M - T_E) + 2n_z q\sin\psi J_1(qr)T_M]dq} \quad (2.25)$$

Now considering only the angular part of (2.23)

$$\mathrm{H}_{t,y}(\theta) = \int_0^{2\pi} e^{iqrcos\theta}[-n_x\kappa_0(\sin^2(\theta+\psi)T_E + \cos^2(\theta+\psi)T_M) - in_z q\cos(\theta+\psi)T_M]d\theta$$

Simplifying the trig we rewrite as

$$\mathrm{H}_{t,y}(\theta) = \int_0^{2\pi} e^{iqrcos\theta}[-\frac{1}{2}n_x\kappa_0(T_E + T_M + (T_M - T_E)\cos[2(\theta+\psi)]) - in_z q(\cos\theta\cos\psi - \sin\theta\sin\psi)T_M]d\theta$$

Expanding the trig and using (B.2) & (B.4)

$$\mathrm{H}_{t,y}(\theta) = 2\pi n_z q \cos\psi J_1(qr) T_M + \int_0^{2\pi} e^{iqr\cos\theta}[-\frac{1}{2} n_x \kappa_0 (T_E + T_M + (T_M - T_E)(\cos(2\theta)\cos(2\psi) - \sin(2\theta)\sin(2\psi))]d\theta$$

Simplifying using (B.1), (B.3), and (B.5) and combining with the rest of (2.23)

$$\boxed{\mathrm{H}_{t,y} = \int_0^{\infty} \pi\alpha q e^{-\kappa_0 z}[-n_x\kappa_0[J_0(qr)(T_E + T_M) + J_2(qr)(T_E - T_M)\cos(2\psi)] + 2n_z q\cos\psi J_1(qr) T_M]dq} \tag{2.26}$$

Now considering only the angular part of (2.24)

$$\mathrm{H}_{t,z}(\theta) = \int_0^{2\pi} e^{iqr\cos\theta}[-in_x q(\sin\theta\cos\psi + \sin\psi\cos\theta)]d\theta$$

Simplifying with (B.2) & (B.4) and combining with the rest of (2.24)

$$\boxed{\mathrm{H}_{t,z} = \int_0^{\infty} 2\pi\alpha q^2 e^{-\kappa_0 z} n_x \sin\psi J_1(qr) T_E dq} \tag{2.27}$$

2.2.5 Analysis of the Transmitted Field

We analyzed the transmitted H-field by numerically evaluating at

$$|\mathbf{H}_t| = \sqrt{|\mathrm{H}_{t,x}|^2 + |\mathrm{H}_{t,y}|^2 + |\mathrm{H}_{t,z}|^2} \tag{2.28}$$

If we consider the case where the souce is polarized perpendicular to the slab, i.e.

$n_x = 0, n_z = 1$, inspecting (2.25), (2.26), and (2.27) we see the field becomes

$$\mathrm{H}_{t,x} = -2\pi \sin\psi \int_0^\infty \alpha q^2 e^{-\kappa_0 z} J_1(qr) T_M dq \tag{2.29}$$

$$\mathrm{H}_{t,y} = 2\pi \cos\psi \int_0^\infty \alpha q^2 e^{-\kappa_0 z} J_1(qr) T_M dq \tag{2.30}$$

and $\mathrm{H}_{t,z} = 0$, evaluating $|\mathbf{H}_t|$ yields

$$|\mathbf{H}_t| = \sqrt{(4\pi \sin^2\psi + 4\pi \cos^2\psi) \left| \int_0^\infty \alpha q^2 e^{-\kappa_0 z} J_1(qr) T_M dq \right|^2}$$

$$|\mathbf{H}_t| = 2\pi \left| \int_0^\infty \alpha q^2 e^{-\kappa_0 z} J_1(qr) T_M dq \right| \tag{2.31}$$

We note that (2.31) exhibits radial symmetry in the xy plane, thus one simply needs to evaluate the field along a radius to obtain all of the information stored in the field. Furthermore, we note that any dependence on T_E and thus $\delta\mu$, has dropped out; and in this polarization only, the field is only dependant on $\delta\epsilon$. A typical field profile is shown in Fig. 2.2, and one can see that a dipole thus polarized in this manner is resolved in a series of concentric rings with the unexpected feature that $|\mathbf{H}_t| = 0$ at at the center. We note the close resemblence to an Airy disk, although there was no hole in the slab!

We may also investigate how the field evolves as we move away from the slab, that is to say, the z dependence of the transmitted field, for which a typical field profile is shown in Fig. 2.3. One thing to notice is that because the main contribution comes from the evanescent field $|\mathbf{H}_t|$ decays like $e^{-\kappa_0 z}$ as is seen in (2.25), (2.26), & (2.27), this exponentially decaying behavior is clearly seen in Fig. 2.3 (Left). To avoid this background change and to confirm where the focus occurs we normalize

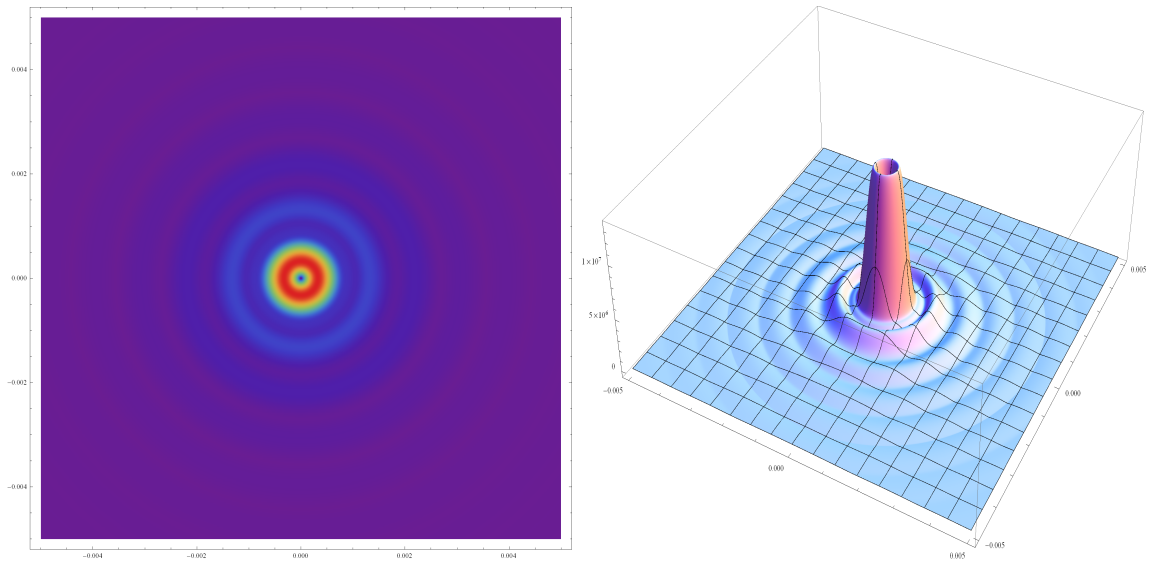

Figure 2.2: (Left) Density Plot and (Right) 3D Plot of $|\mathbf{H}_t|$ in the focal plane z=$\frac{3}{2}d$

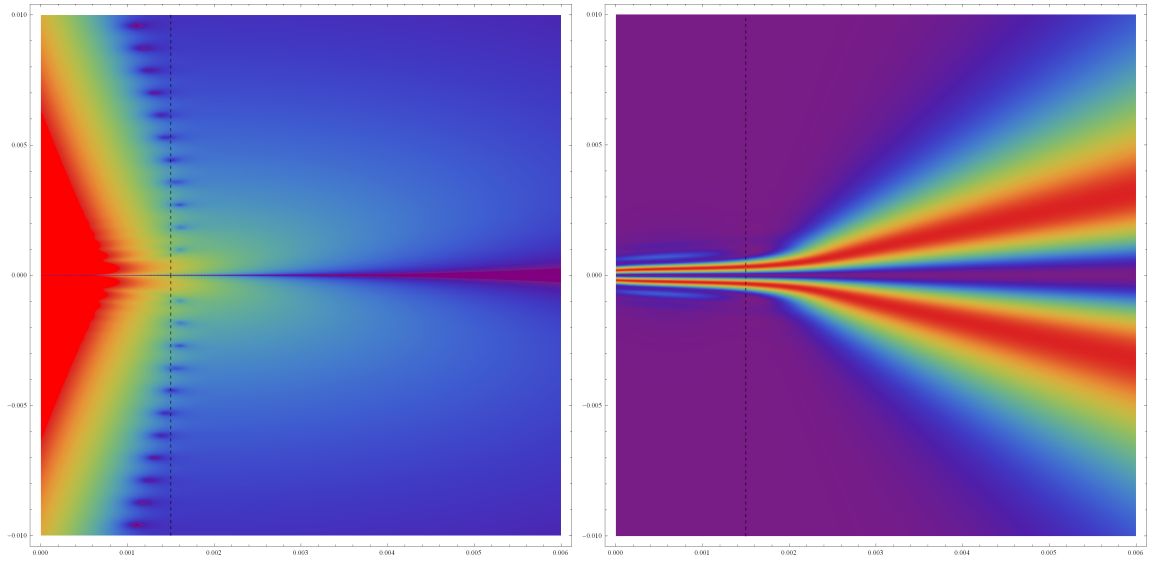

Figure 2.3: The z dependence of the transmitted field for the point source geometry, the dashed line shows the focal plane of $z = \frac{3}{2}d$. (Left) $\ln|\mathbf{H}_t|$ (Right) $|\mathbf{H}_t(z,x)/\max[[\mathbf{H}_t(z)]]|^2$

the field by its maximal strength for each value of z, in Fig. 2.3 (Right) we plot $|\mathbf{H}_t(z,x)/\max[\mathbf{H}_t(z)]|^2$.

We note the close similarity of Fig. 2.3 (Right) to the normalized field show in [28], with the obvious difference being that in this geometry the field goes to zero the at center. Fig. 2.3 (Right) clearly confirms that the focal plane is the plane of $z = \frac{3}{2}d$. This result can be derived using Snell's law, and is shown to be independent of the refractive index. One final thing to observe is that the ridges that appear in these plots are just another manfestation of the rings shown in Fig. 2.2, and thus we see that they exist for all z, albeit with variable relative magnitudes.

By using a linear combination of $\mathbf{H}$ when $n_x = 0$ and when $n_x = 1$, we explored other polarizations of the source. We define θ_P to be the angle between $\hat{\mathbf{n}}$ and the z-axis or $\theta_p = \arctan\left(\frac{n_x}{n_z}\right)$. As can be seen in Fig. 2.4 although the field profile

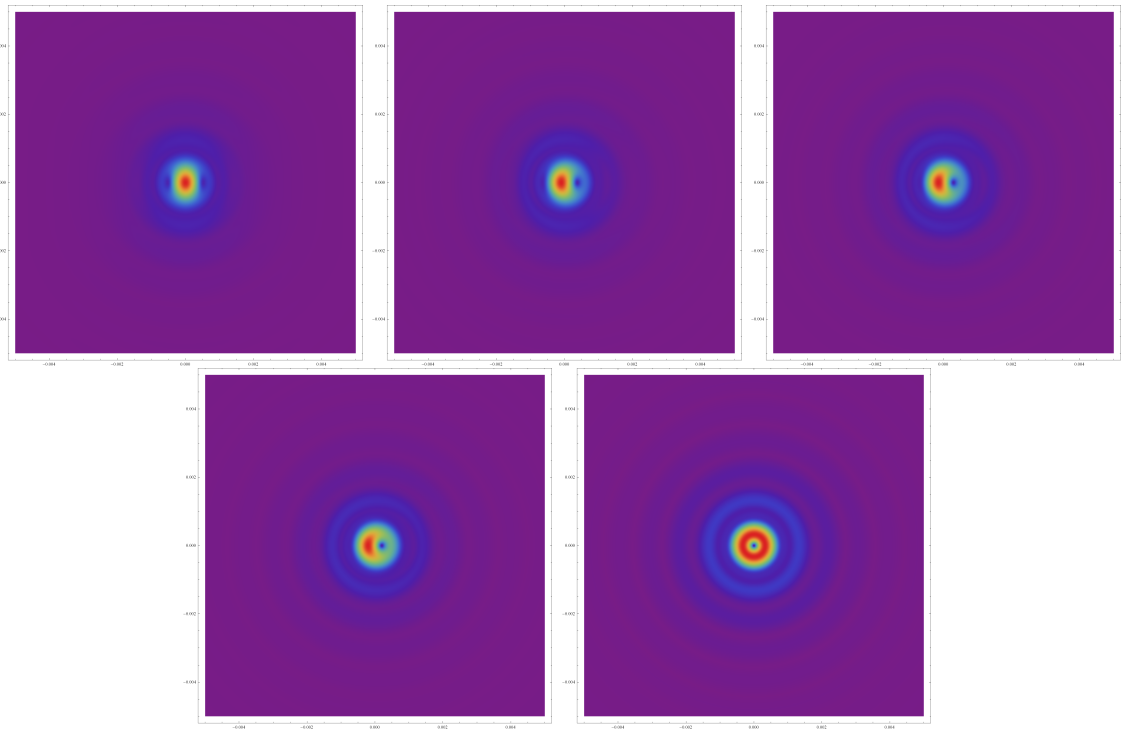

Figure 2.4: $|\mathbf{H}_t|$ in the focal plane $z = \frac{3}{2}d$. Top row, left to right, $\theta_P = 90°, 60°, 45°$, and in the bottom row, left to right $\theta_P = 30°, 0°$

changes slightly for different polarizations, the resolution is not strongly dependent

on the source polarization.

In the focal plane the tranmitted field largley exists within a very confined region, this is most easily seen in Fig. 2.2 (Right). For simplicity we restrict our further analysis to the case where the souce is polarized perpendicular to the slab, and is therefore only dependent on $\delta\epsilon$. If we define the resolution length L_R as the distance from the origin to the first minimum of the field, we find that the resolution is in excellent agreement with the result derived by Merlin [26] and others for a slightly different geometry, and will be derived analytically in section 2.3

$$L_R \approx -\frac{2\pi d}{\ln|\delta\epsilon/2|} \tag{2.32}$$

All of the figures in this part of the paper were calculated with $\delta\epsilon = \delta\mu = (1+i)10^{-3}$ and with $\lambda/d \approx 190$, using (2.32) gives $\lambda/L_R \approx 220$ which is extremely close to the numerically calculated vlaue. Fig. 2.5 shows a comparison between (2.32) and

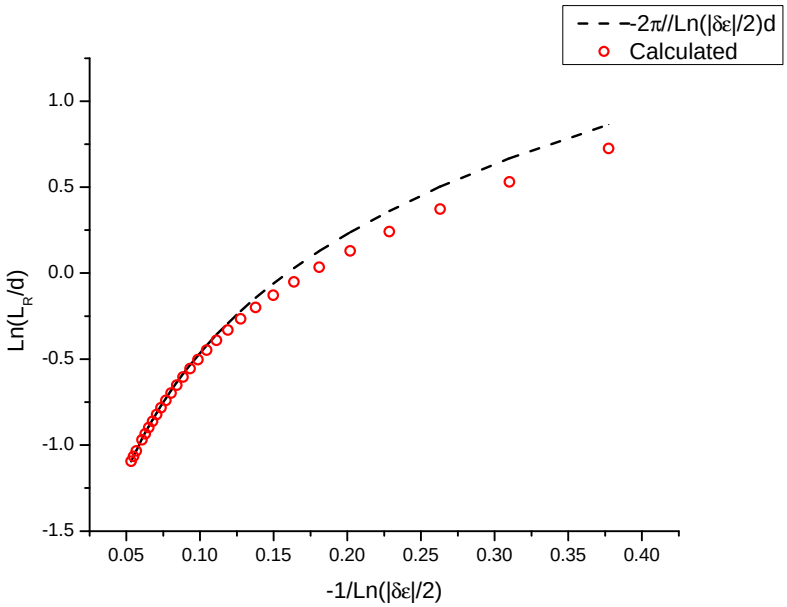

Figure 2.5: Comparison of the numerically calculated resolution length with (2.32) as a function of $\delta\epsilon$

the numerically calculated value as a function of $\delta\epsilon$. As can be expected from the

assumptions made in the derivation of (2.32), the agreement is almost perfect for very small $\delta\epsilon$ and only begins to disagree for large $\delta\epsilon$, with the disagreement being unexpectedly small. The main conclusion is thus the same as was conlcuded earlier [26], that although the resolution is strongly limited by the logarithmic dependence on $\delta\epsilon$, given precise enough control over the material's permitivity and thickness, one can achieve arbitrarily good resolution.

2.3 Line Dipole Source

Remarkably an analytical solution to the problem exists in two dimensions when we replace the point dipole source with a line of parallel dipoles. In this section by also considering the presence of small losses we expand on the results first published by Merlin [26] in 2004 while detailing their derivation.

2.3.1 Source Field

We first briefly outline the set-up found in [26] before begining the more detailed integration and analysis.

For simplicity we take $\delta\mu = 0$. The source is a a uniform line of dipoles placed on the z axis at $z = -d/2$, which for one orientation, has current density $\mathbf{j} = p\delta(x)\delta(z + d/2)e^{i\omega t}\hat{\mathbf{x}}$. The transverse magnetic solutions to Maxwell's equations are of the form $\mathrm{H}_y = h(z)e^{i(qx-\omega t)}, \mathrm{H}_x = \mathrm{H}_z = 0$. Note that because the transmission functions are nearly identical, only a few modifications are necessary to the following derivation to hande transverse electric fields.

The source magnetic field can be written as the sum of a propogating radiative component, for which $|q| < \omega/c$ and an evanesent near-field, for which $|q| > \omega/c$, thus

$$\mathrm{H}_{s,y} = \int_{-\infty}^{\infty} \mathcal{H}(q)e^{iqx-\kappa_0(z+d/2)}dq \tag{2.33}$$

Where $\mathcal{H}(q) = -sgn(z + d/2)p/c$, substituting (2.2) and defining $k_0 \equiv \omega/c$ yields

$$\mathrm{H}_{s,y}^{R} = \int_{-k_0}^{k_0} \mathcal{H}(q) e^{iqx + i\sqrt{k_0^2 - q^2}(z+d/2)} dq \tag{2.34}$$

$$\mathrm{H}_{s,y}^{NF} = \int_{|q|>k_0} \mathcal{H}(q) e^{iqx - \sqrt{q^2 - k_0^2}(z+d/2)} dq \tag{2.35}$$

2.3.2 Construction of the Transmitted Field

Consistent with the discussion of the point dipole source the main contribution to the transmitted field comes from the evanescent modes, thus we focus our attention to the near-field. Noting that the derivation of transmission functions in section 2.2.3 is general enough to apply to this geometry

$$\mathrm{H}_{t,y}^{NF} = -\frac{p}{c} \int_{|q|>k_0} T_M e^{iqx - \kappa_0 z} dq \tag{2.36}$$

Substituting (2.18) and defining $u \equiv \frac{3}{2}d - z$, we obtain

$$\mathrm{H}_{t,y}^{NF} = -\frac{p}{c} \int_{|q|>k_0} \frac{4\kappa\kappa_0\epsilon e^{\kappa_0 d/2}}{(\kappa + \epsilon\kappa_0)^2 e^{\kappa d} - (\kappa - \epsilon\kappa_0)^2 e^{-\kappa d}} e^{-3\kappa_0 d/2} e^{iqx + \kappa_0 u} dq \tag{2.37}$$

In order to analytically integrate (2.37) we divide the integral into two regions: (i) $k_0 < |q| < Q$ and (ii) $|q| > Q$, where Q is an auxiliary variable which satisfies: $k_0 \ll Q \ll q_0 = \frac{1}{d}\ln\frac{1}{|\delta\epsilon|}$. Thus we write

$$H_{t,y}^{NF} = H^{(i)} + H^{(ii)} \tag{2.38}$$

2.3.2.1 Integration of region (i) $k_0 < |q| < Q$

In this region we set $\delta\epsilon = 0$ which as shown by Pendry using a different method [24] and Merlin [26], $T_M \approx e^{3\kappa_0 d/2}$, therefore

$$\mathrm{H}^{(i)} \approx -\frac{p}{c} \int\limits_{k_0<|q|<Q} e^{iqx+\kappa_0 u} dq \tag{2.39}$$

We break (2.39) into the seperate cases: $u > 0$ & $u < 0$

- $u > 0$

Recalling (2.2) $\kappa_0 = \sqrt{q^2 - \omega^2/c^2}$ and noting that in region (i) by definition $q > w/c = k_0$ and furthermore that the main contribution from the integral comes from large $q \Rightarrow q \gg k_0 \Rightarrow \kappa_0 \approx |q|$, therefore the integral simplifies as

$$\mathrm{H}^{(i)}(u>0) = \int\limits_{k_0<|q|<Q} e^{iqx+\kappa_0 u} dq \approx \int\limits_{k_0<|q|<Q} e^{iqx+|q|u} dq = \int\limits_{k_0}^{Q} e^{(ix+u)q} dq + \int\limits_{-Q}^{-k_0} e^{(ix-u)q} dq$$

$$\mathrm{H}^{(i)}(u>0) = 2\frac{e^{Qu}[u\cos(Qx) + x\sin(Qx)] - e^{k_0 u}[u\cos(k_0 x) + x\sin(k_0 x)]}{u^2 + x^2} \tag{2.40}$$

- $u < 0$

In this case we break up the integral into two regions as follows

$$\int\limits_{k_0<|q|<Q} e^{iqx+\kappa_0 u} dq = \int\limits_{|q|>k_0} e^{iqx+\kappa_0 u} dq - \int\limits_{|q|>Q} e^{iqx+\kappa_0 u} dq \tag{2.41}$$

In evaluating the integral over $|q| > Q$ we make the same approximation that $\kappa_0 \approx |q|$

$$\int\limits_{|q|>Q} e^{iqx+\kappa_0 u} dq \approx \int\limits_{Q}^{\infty} e^{(ix+u)q} dq + \int\limits_{-\infty}^{-Q} e^{(ix-u)q} dq = -2e^{Qu}\frac{u\cos(Qx) + x\sin(Qx)}{u^2 + x^2} \tag{2.42}$$

In evaluating the integral over $|q| > k_0$ we can integrate exactly yielding

$$\int_{|q|>k_0} e^{iqx+\kappa_0 u} dq = \pi N_1 \left[k_0\sqrt{u^2+x^2}\right] \frac{k_0 u}{\sqrt{u^2+x^2}} - \int_{-k_0}^{k_0} \cos(qx)\cos\left[u\sqrt{k_0^2-q^2}\right] dq \tag{2.43}$$

Where N_1 is a Neumann function. Combining these results yields

$$\mathrm{H}^{(i)} \approx \begin{cases} -2\frac{p}{c}\frac{e^{Qu}[u\cos(Qx)+x\sin(Qx)] - e^{k_0 u}[u\cos(k_0 x)+x\sin(k_0 x)]}{u^2+x^2} & u>0 \\ -\pi\frac{p}{c}N_1\left[k_0\sqrt{u^2+x^2}\right]\frac{k_0 u}{\sqrt{u^2+x^2}} - 2\frac{p}{c}e^{Qu}\frac{u\cos(Qx)+x\sin(Qx)}{u^2+x^2} & \\ \qquad +\frac{p}{c}\int_{-k_0}^{k_0}\cos(qx)\cos\left[u\sqrt{k_0^2-q^2}\right]dq & u<0 \end{cases} \tag{2.44}$$

2.3.2.2 Integration of region (ii) $|q| > Q$

In region (ii) we approximate T_M by noting that $q \gg k_0$ and thus in the exponentials we set $\kappa \approx \kappa_0 \approx |q|$ we then define $\vartheta = \frac{k_0}{q} \ll 1$. Expanding T_M with respect to ϑ and keeping terms up to $\mathcal{O}(\vartheta)$, as shown in [26] we get

$$T_M \approx \frac{e^{3|q|d/2}}{1-\frac{\delta\epsilon^2}{4}e^{2|q|d}} \tag{2.45}$$

Using (2.45) in (2.37), and recalling that in the exponentials we take $\kappa_0 \approx |q|$

$$\mathrm{H}^{(ii)} \approx -\frac{p}{c}\int_{|q|>Q} \frac{e^{3|q|d/2}}{1-\frac{\delta\epsilon^2}{4}e^{2|q|d}} e^{-3|q|d/2} e^{iqx+|q|u} dq = -\frac{p}{c}\left(\int_{-\infty}^{+\infty} - \int_{-Q}^{+Q}\right)\frac{e^{iqx+|q|u}}{1-\frac{\delta\epsilon^2}{4}e^{2|q|d}}dq \tag{2.46}$$

We now define

$$I^{\pm} = \int_0^{\infty} \frac{e^{\pm iqx+qu}}{1-\frac{\delta\epsilon^2}{4}e^{2qd}} dq \tag{2.47}$$

Defining $\beta \equiv qd$ and $v_\pm \equiv v_1 \pm iv_2 \equiv \frac{u}{d} \pm i\frac{x}{d}$, we re-write (2.47) as

$$I^\pm = \frac{1}{d}\int_0^\infty \frac{e^{\beta v_\pm}}{1-\frac{\delta\epsilon^2}{4}e^{2\beta}}d\beta \tag{2.48}$$

We now define

$$\Delta I = \int_{-Q}^{+Q} \frac{e^{iqx+|q|u}}{1-\frac{\delta\epsilon^2}{4}e^{2|q|d}}dq \tag{2.49}$$

Comparing (2.46) to (2.48) & (2.49) we see that

$$H^{(ii)} = -\frac{p}{c}(I^+ + I^- - \Delta I) \tag{2.50}$$

We will now evaluate $I^\pm$ using contour integration

- $I^+(x > 0)$, i.e. $I^+(v_2 > 0)$

Note that $\delta\epsilon \in \mathbb{C} \Rightarrow$ there are no poles on the Real axis, the contour chosen is

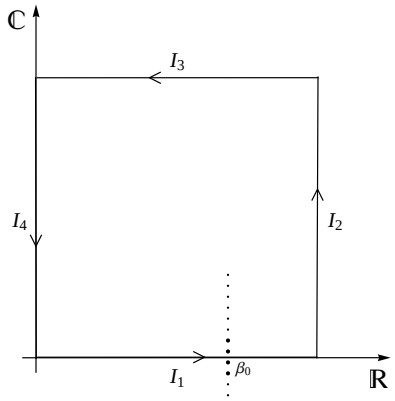

To find the poles we find the value of β_0 that causes (2.48) to become singular

$$0 = 1 - \frac{\delta\epsilon^2}{4}e^{2\beta_0} \Rightarrow \beta_0 = \frac{1}{2}\ln\left(\frac{4}{\delta\epsilon^2}\right)$$

and thus, we see that the poles are $P_n = \beta_0 + in\pi, n \in \mathbb{Z}$. They are all simple poles.

By the residue theorem

$$I_1 + I_2 + I_3 + I_4 = \frac{2\pi i}{d} \sum_n Res(F, P_n) \tag{2.51}$$

Where

$$F(\zeta) = \frac{e^{\zeta v_+}}{1 - \frac{\delta\epsilon^2}{4} e^{2\zeta}} \tag{2.52}$$

$\gg$ **Evaluating** $\sum_n Res(F, P_n)$

Recall that for a simple pole c if $f(x) = \frac{g(x)}{h(x)} \Rightarrow Res(f, c) = \frac{g(c)}{h'(c)}$ for $h'(c) \neq 0$, therefore

$$Res(F, P_n) = \frac{e^{(\beta_0 + in\pi)v_+}}{-2\frac{\delta\epsilon^2}{4} e^{2(\beta_0 + in\pi)}} \tag{2.53}$$

If we consider the denominator of (2.53), we see that by definition it simplifies as

$$-2\frac{\delta\epsilon^2}{4} e^{2(\beta_0 + in\pi)} = -2$$

Thus

$$Res(F, P_n) = -\frac{1}{2} e^{\beta_0 v_+} e^{in\pi v_+} \tag{2.54}$$

Noting that the poles within the contour path are for $n \in \mathbb{Z}^+$ and plugging in (2.54) we see

$$\frac{2\pi i}{d} \sum_n Res(F, P_n) \to -\frac{\pi i}{d} \sum_{n=1}^{\infty} e^{\beta_0 v_+} e^{in\pi v_+} = \frac{\pi i}{d} \frac{e^{i\pi v_+}}{-1 + e^{i\pi v_+}} e^{\beta_0 v_+} \tag{2.55}$$

Noting that

$$e^{\beta_0 v_+} = e^{\frac{1}{2}\ln\left(\frac{4}{\delta\epsilon^2}\right) v_+} = \left(\frac{4}{\delta\epsilon^2}\right)^{\frac{v_+}{2}} \tag{2.56}$$

Plugging (2.56) into (2.55) yields

$$\frac{2\pi i}{d}\sum_n Res(F,P_n) = \frac{1}{d}\frac{i\pi}{1-e^{-i\pi v_+}}\left(\frac{4}{\delta\epsilon^2}\right)^{\frac{v_+}{2}} \tag{2.57}$$

$\gg$ **Evaluating** I_1

$$I_1 = \lim_{R\to\infty}\frac{1}{d}\int_0^R F(\zeta)d\zeta = I^+(x>0) \tag{2.58}$$

$\gg$ **Evaluating** I_2

Along this path $\zeta = R+iy \Rightarrow d\zeta = idy$

$$I_2 = \lim_{R\to\infty}\frac{1}{d}\int_0^R F(\zeta)d\zeta = \lim_{R\to\infty}\frac{i}{d}\int_0^R G(y)dy \tag{2.59}$$

Substituting (2.52) and recalling the definition of v_+

$$F(\zeta) = \frac{e^{(R+iy)(v_1+iv_2)}}{1-\frac{\delta\epsilon^2}{4}e^{2(R+iy)}} = G(y) \tag{2.60}$$

Rearranging slightly and making use of the triangle inequaltiy in the denominator, we note that

$$|G(y)| = \left|\frac{e^{Rv_1-yv_2}e^{i(Rv_2+yv_1)}}{1-\frac{\delta\epsilon^2}{4}e^{2(R+iy)}}\right| < \frac{e^{Rv_1-yv_2}}{|\frac{|\delta\epsilon|^2}{4}e^{2R}-1|}$$

In this region $y \geq 0$ & $v_2 > 0$, therefore

$$\lim_{R\to\infty}\frac{e^{Rv_1-yv_2}}{|\frac{|\delta\epsilon|^2}{4}e^{2R}-1|} = \lim_{R\to\infty}\frac{e^{Rv_1}}{e^{2R}} = \lim_{R\to\infty}e^{R(v_1-2)}$$

Recalling that $v_1 = \frac{u}{d} = \frac{\frac{3}{2}d-z}{d} = \frac{3}{2}-\frac{z}{d}$, for all $z > d$, i.e. the transmitted field,

$v_1 < \frac{1}{2} \Rightarrow v_1 - 2 < -1.5 \Rightarrow$ the limit converges and thus

$$\lim_{R\to\infty} e^{R(v_1-2)} = 0$$

Putting it all together we see that

$$\lim_{R\to\infty} \left| \frac{i}{d} \int_0^R G(y)dy \right| < 0 \tag{2.61}$$

Applying the Squeeze Theorem yields

$$I_2 = \lim_{R\to\infty} \frac{i}{d} \int_0^R G(y)dy = 0 \tag{2.62}$$

$\gg$ **Evaluating** I_3

Along this path $\zeta = y + iR \Rightarrow d\zeta = dy$

$$I_3 = \lim_{R\to\infty} \frac{1}{d} \int_0^R F(\zeta)d\zeta = \lim_{R\to\infty} \frac{1}{d} \int_R^0 H(y)dy \tag{2.63}$$

Definging $H(y)$ analogously as in (2.60) we note that

$$\left| \int_R^0 H(y)dy \right| \leq \int_0^R |H(y)|dy = \int_0^R \left| \frac{e^{y+iR}e^{v_1+iv_2}}{1 - \frac{\delta\epsilon^2}{4}e^{2(y+iR)}} \right| dy$$

$$= \int_0^R \frac{e^{yv_1 - Rv_2}}{|1 - \frac{\delta\epsilon^2}{4}e^{2(y+iR)}|} dy < \int_0^R \frac{e^{yv_1 - Rv_2}}{|\frac{|\delta\epsilon|^2}{4}e^{2y} - 1|} dy$$

We now break the integral into two regions

$$\int_0^R \frac{e^{yv_1 - Rv_2}}{|\frac{|\delta\epsilon|^2}{4}e^{2y} - 1|}dy = e^{-Rv_2}\left(\int_0^{\ln\frac{2}{|\delta\epsilon|}} + \int_{\ln\frac{2}{|\delta\epsilon|}}^R\right)\frac{e^{yv_1}}{|\frac{|\delta\epsilon|^2}{4}e^{2y} - 1|}dy \tag{2.64}$$

We observe that the integral of the first region in (2.64) is dominated by the numerator because $0 < y < \ln\frac{2}{\delta\epsilon} \Rightarrow \frac{|\delta\epsilon|^2}{4}e^{2y} < 1$ and that the integral of the second region is dominated by both exponential terms. Thus we see that

$$\left|\int_R^0 H(y)dy\right| < e^{-Rv_2}\left(\int_0^{\ln\frac{2}{|\delta\epsilon|}} e^{yv_1}dy + \int_{\ln\frac{2}{|\delta\epsilon|}}^R e^{y(v_1-2)}dy\right) \tag{2.65}$$

By similar arguments as above, we see that

$$\lim_{R\to\infty} e^{-Rv_2}\left(\int_0^{\ln\frac{2}{|\delta\epsilon|}} e^{yv_1}dy + \int_{\ln\frac{2}{|\delta\epsilon|}}^R e^{y(v_1-2)}dy\right) = 0 \tag{2.66}$$

Putting it all together we see that

$$\lim_{R\to\infty}\left|\frac{1}{d}\int_R^0 H(y)dy\right| < 0 \tag{2.67}$$

Applying the Squeeze Theorem yields

$$I_3 = \lim_{R\to\infty}\frac{1}{d}\int_R^0 H(y)dy = 0 \tag{2.68}$$

$\gg$ **Evaluating** I_4

Along this path $\zeta = iy \Rightarrow d\zeta = idy$, therefore we can write

$$I_4 = \lim_{R\to\infty} \frac{1}{d} \int_0^R F(\zeta) d\zeta = \lim_{R\to\infty} \frac{i}{d} \int_R^0 \frac{e^{iy(v_1+iv_2)}}{1 - \frac{\delta\epsilon^2}{4} e^{2iy}} dy \tag{2.69}$$

Because $|\delta\epsilon| \ll 1 \Rightarrow 1 - \frac{\delta\epsilon^2}{4} e^{2iy} \approx 1$, we approximate the integral as

$$I_4 \approx \frac{i}{d} \int_\infty^0 e^{y(iv_1 - v_2)} dy = \frac{-i}{d(v_2 - iv_1)} = \frac{1}{d(v_1 + iv_2)} \tag{2.70}$$

Thus, recalling $v_+ = v_1 + iv_2$, we see that

$$I_4 \approx \frac{1}{dv_+} \tag{2.71}$$

Recalling the Residue Theorem (2.51)

$$I_1 + I_2 + I_3 + I_4 = \frac{2\pi i}{d} \sum_n Res(F, P_n)$$

Plugging I_1 (2.57), I_2 (2.58), I_3 (2.62), I_4 (2.68), & $\sum_n Res(F, P_n)$ (2.71) into (2.51) yields

$$I^+(x > 0) + \frac{1}{dv_+} \approx \frac{1}{d} \frac{i\pi}{1 - e^{-i\pi v_+}} \left(\frac{4}{\delta\epsilon^2} \right)^{\frac{v_+}{2}}$$

Thus

$$I^+(x > 0) \approx \frac{1}{d} \left[\frac{i\pi}{1 - e^{-i\pi v_+}} \left(\frac{4}{\delta\epsilon^2} \right)^{\frac{v_+}{2}} - \frac{1}{v_+} \right] \tag{2.72}$$

- $I^+(x < 0)$, i.e. $I^+(v_2 < 0)$

We now choose the following contour path. Following the same procedure as for $I^+(x > 0)$ one can obtain the following results, however we won't show their derivations because we take the analogy to be obvious from symmetry arguments. Therefore

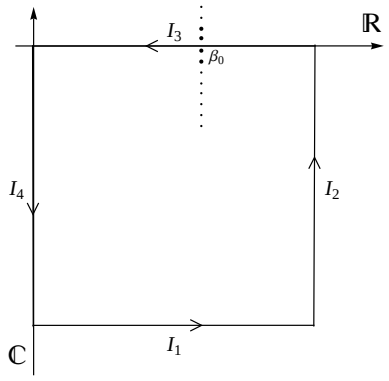

for $x < 0$

$$I_1 = I_2 = 0 \qquad I_3 = -I^+(x < 0) \qquad I_4 \approx -\frac{1}{dv_+} \tag{2.73}$$

Similarly

$$\frac{2\pi i}{d} \sum_n Res(F, P_n) = -\frac{1}{d} \frac{i\pi}{1 - e^{-i\pi v_+}} \left(\frac{4}{\delta \epsilon^2} \right)^{\frac{v_+}{2}} \tag{2.74}$$

Plugging into the Residue Theorem (2.51) yields

$$I^+(x < 0) \approx \frac{1}{d} \left[\frac{i\pi}{1 - e^{-i\pi v_+}} \left(\frac{4}{\delta \epsilon^2} \right)^{\frac{v_+}{2}} - \frac{1}{v_+} \right] = I^+(x > 0) \tag{2.75}$$

Thus we see that I^+ is the same for $x > 0$ and $x < 0$ and that for all x

$$I^+ \approx \frac{1}{d} \left[\frac{i\pi}{1 - e^{-i\pi v_+}} \left(\frac{4}{\delta \epsilon^2} \right)^{\frac{v_+}{2}} - \frac{1}{v_+} \right] \tag{2.76}$$

- $I^-(x > 0)$ and $I^-(x < 0)$

We choose the following contour paths for $I^-(x > 0)$ and $I^-(x < 0)$ respectivley.

Note that these paths are identical to the ones used for I^+, except that they have been switched for $x < 0$ and $x > 0$, explicitly the path for $I^+(x > 0) \to I^-(x < 0)$ and similarly $I^+(x < 0) \to I^-(x > 0)$. Thus as before if one carefully carries out the integration along these paths they will arrive at the results that we take to be

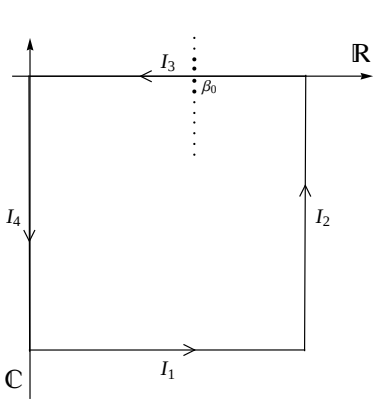

$I^-(x > 0)$

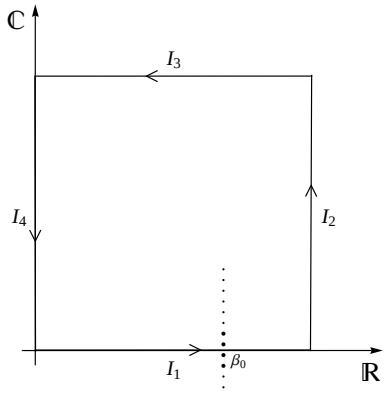

$I^-(x < 0)$

obvious from symmetry arguments, in summary

$$I^- \approx \frac{1}{d}\left[\frac{i\pi}{1-e^{-i\pi v_-}}\left(\frac{4}{\delta\epsilon^2}\right)^{\frac{v_-}{2}} - \frac{1}{v_-}\right] \tag{2.77}$$

Putting (2.76) & (2.77) together we see that

$$I^\pm \approx \frac{1}{d}\left[\frac{i\pi}{1-e^{-i\pi v_\pm}}\left(\frac{4}{\delta\epsilon^2}\right)^{\frac{v_\pm}{2}} - \frac{1}{v_\pm}\right] \tag{2.78}$$

- **Evaluating ΔI**

Recall (2.49)

$$\Delta I = \int_{-Q}^{+Q} \frac{e^{iqx+|q|u}}{1-\frac{\delta\epsilon^2}{4}e^{2|q|d}}dq$$

We defined $Q \ll q_0 = \frac{1}{d}\ln\frac{1}{|\delta\epsilon|} \Rightarrow 1 - \frac{\delta\epsilon^2}{4}e^{2|q|d} \approx 1$. Following a similar argument as the one that was used to obtain (2.40) we obtain

$$\Delta I \approx 2\int_0^Q \cos(qx)e^{qu}dq \tag{2.79}$$

Integrating (2.79) yields

$$\Delta I \approx -2\frac{u - e^{Qu}[u\cos(Qx) + x\sin(Qx)]}{u^2 + x^2} \tag{2.80}$$

Putting it all together we plug $I^{\pm}$ (2.78) & ΔI (2.80) into $H^{(ii)}$ (2.50) to obtain

$$\begin{aligned} H^{(ii)} \approx -\frac{p}{c}\frac{1}{d}\left[\frac{i\pi}{1 - e^{-i\pi v_{\pm}}}\left(\frac{4}{\delta\epsilon^2}\right)^{\frac{v_{\pm}}{2}} - \frac{1}{v_{\pm}}\right] \\ - 2\frac{p}{c}\frac{u - e^{Qu}[u\cos(Qx) + x\sin(Qx)]}{u^2 + x^2} \end{aligned} \tag{2.81}$$

We then plug $H^{(i)}$ (2.44) and $H^{(ii)}$ (2.81) into $H^{NF}_{t,y}$ (2.38) to obtain

$$\begin{aligned} H^{NF}_{t,y} \approx -\frac{p}{c}\frac{1}{d}\left[\frac{i\pi}{1 - e^{-i\pi v_{\pm}}}\left(\frac{4}{\delta\epsilon^2}\right)^{\frac{v_{\pm}}{2}} - \frac{1}{v_{\pm}}\right] \\ - 2\frac{p}{c}\frac{u - e^{Qu}[u\cos(Qx) + x\sin(Qx)]}{u^2 + x^2} + \\ \begin{cases} -2\frac{p}{c}\frac{e^{Qu}[u\cos(Qx) + x\sin(Qx)] - e^{k_0 u}[u\cos(k_0 x) + x\sin(k_0 x)]}{u^2 + x^2} & u > 0 \\ -\pi\frac{p}{c}N_1\left[k_0\sqrt{u^2 + x^2}\right]\frac{k_0 u}{\sqrt{u^2 + x^2}} - 2\frac{p}{c}e^{Qu}\frac{u\cos(Qx) + x\sin(Qx)}{u^2 + x^2} & \\ \qquad + \frac{p}{c}\int_{-k_0}^{k_0}\cos(qx)\cos\left[u\sqrt{k_0^2 - q^2}\right]dq & u < 0 \end{cases} \end{aligned} \tag{2.82}$$

Canceling some terms we see that the auxillary variable Q drops out to give

$$H_{t,y}^{NF} \approx -\frac{p}{c}\frac{1}{d}\left[\frac{i\pi}{1-e^{-i\pi v_\pm}}\left(\frac{4}{\delta\epsilon^2}\right)^{\frac{v_\pm}{2}} - \frac{1}{v_\pm}\right] - 2\frac{p}{c}\frac{u}{u^2+x^2} \quad +$$
$$\begin{cases} 2\frac{p}{c}e^{k_0 u}\frac{u\cos(k_0 x)+x\sin(k_0 x)}{u^2+x^2} & u>0 \\ -\pi\frac{p}{c}N_1\left[k_0\sqrt{u^2+x^2}\right]\frac{k_0 u}{\sqrt{u^2+x^2}} + \frac{p}{c}\int\limits_{-k_0}^{k_0}\cos(qx)\cos\left[u\sqrt{k_0^2-q^2}\right]dq & u<0 \end{cases} \tag{2.83}$$

Furthermore recalling the definition of $v_\pm$, we observe that

$$\frac{1}{dv_\pm} = \frac{1}{d}\left[\frac{1}{v_+}+\frac{1}{v_-}\right] = \frac{1}{d}\left[\frac{1}{\frac{u}{d}+i\frac{x}{d}}+\frac{1}{\frac{u}{d}-i\frac{x}{d}}\right] \Rightarrow$$
$$\frac{1}{dv_\pm} = \frac{2u}{u^2+x^2} \tag{2.84}$$

Putting (2.84) back into (2.83) gives

$$\frac{c}{p}H_{t,y}^{NF} \approx -\frac{1}{d}\frac{i\pi}{1-e^{-i\pi v_\pm}}\left(\frac{4}{\delta\epsilon^2}\right)^{\frac{v_\pm}{2}} +$$
$$\begin{cases} 2e^{k_0 u}\frac{u\cos(k_0 x)+x\sin(k_0 x)}{u^2+x^2} & u>0 \\ -\pi N_1\left[k_0\sqrt{u^2+x^2}\right]\frac{k_0 u}{\sqrt{u^2+x^2}} + \int\limits_{-k_0}^{k_0}\cos(qx)\cos\left[u\sqrt{k_0^2-q^2}\right]dq & u<0 \end{cases} \tag{2.85}$$

We can simplify further by noting

$$\frac{i}{1-e^{-i\pi v_\pm}} = \frac{1}{2}\cot(\frac{\pi}{2}v_\pm) + \frac{i}{2} \tag{2.86}$$

Realling the definitions of $v_\pm$ and k_0, and expanding we obtain the final expression

for the transmitted near field

$$\boxed{\begin{aligned}\frac{c}{p}H_{t,y}^{NF} \approx -\frac{\pi}{2d}\Bigg\{&\cot\left[\frac{\pi}{2d}(u+ix)\right]\left(\frac{4}{\delta\epsilon^2}\right)^{\frac{u+ix}{2d}} \\ &+\cot\left[\frac{\pi}{2d}(u-ix)\right]\left(\frac{4}{\delta\epsilon^2}\right)^{\frac{u-ix}{2d}} + i\left[\left(\frac{4}{\delta\epsilon^2}\right)^{\frac{u+ix}{2d}} + \left(\frac{4}{\delta\epsilon^2}\right)^{\frac{u-ix}{2d}}\right]\Bigg\} \\ +\begin{cases} 2e^{u\omega/c}\dfrac{u\cos(\frac{\omega}{c}x)+x\sin(\frac{\omega}{c}x)}{u^2+x^2} & u>0 \\ -\pi N_1\left[\dfrac{\omega}{c}\sqrt{u^2+x^2}\right]\dfrac{\omega u/c}{\sqrt{u^2+x^2}} + \displaystyle\int_{-\frac{\omega}{c}}^{\frac{\omega}{c}}\cos(qx)\cos\left[u\sqrt{\frac{\omega^2}{c^2}-q^2}\right]dq & u<0 \end{cases}\end{aligned}} \tag{2.87}$$

2.3.3 Analysis of the Transmitted Field

A typical field profile is shown in Fig. 2.6, and in the plot on the right, like in

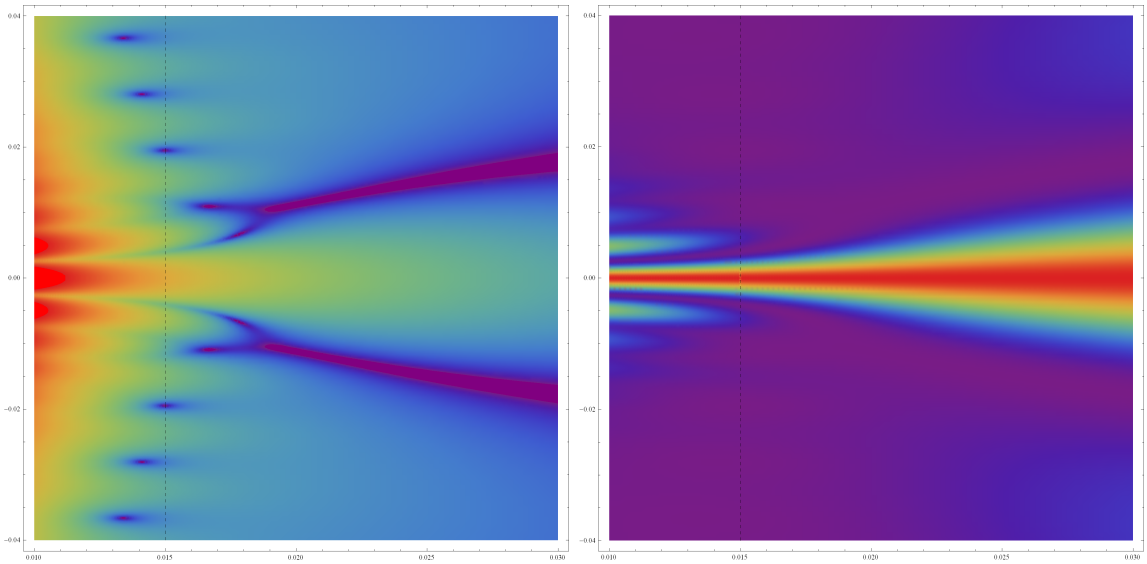

Figure 2.6: The z dependence of the transmitted field for the line source geometry, the dashed line shows the focal plane of $z = \frac{3}{2}d$. (Left) $\ln|\mathbf{H}_t^{NF}|$ (Right) $|\mathbf{H}_t^{NF}(z,x)/\mathbf{H}_t^{NF}(z,0)|^2$

Fig. 2.3, to avoid the background change and to clearly confirm where the focus occurs we normalize the field by its maximal strength for each value of z, which in the line source geometry ocurs at $x = 0$. Again we note the presence of fringes and

the ability of the slab to focus to subwavelength dimensions given a small enough $\delta\epsilon$. A typical field profile in the focal plane is shown in Fig. 2.7. We note that the

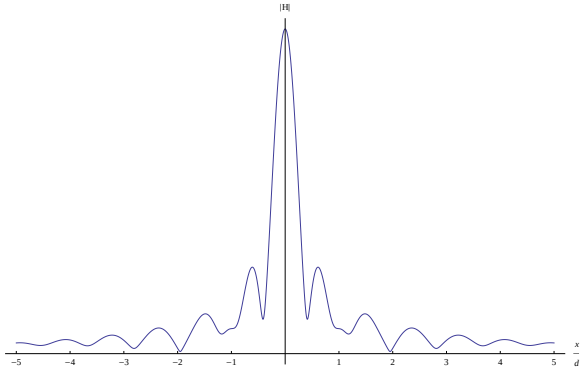

Figure 2.7: Typical field profile of $|\mathbf{H}_t^{NF}|$ in the focal plane of $z = \frac{3}{2}d$

decaying oscillations produce the fringes in Fig. 2.6. Also we also note that there is a striking simliarity to the radial profile for the point source geometry, the peak's non-monotonic heights being quite similar, the biggest difference being that in this geometry the field is maximal at the center, whereas for the point source the field is zero at the center. Furthermore we note that the field never actually reaches zero and this is a major difference between the lossy case considered here and the lossless case derived in section 2.3.4.

One very curious feature of this field is that is has an infinite number of focal planes. This is most clearly seen in the final expression for the transmitted near field (2.87). The multiple focii come from the $\cot\left[\frac{\pi}{2d}(u - ix)\right]$ terms, from which we can read off that it is periodic in u and thus in z with a period of $2d$. However because the field drops off exponentially in z the first focus at $z = \frac{3}{2}d$ is the most important.

2.3.4 Lossless case

In this section we consider the lossless case where $\delta\epsilon_2 = 0$, as was originlly presented in [26]. Note that it is not sufficient to take the limit of (2.87) with $\delta\epsilon_2 \to 0$ because the integration that was performed in section 2.3.2.2 explicitly assumed that

there were no poles on the Real axis. This derivation is essentially the same as for the lossy case, except that we now consider an additional path I_5 along $\beta = \beta_0 + \delta e^{i\theta}$ where $\theta \in [\pi, 0]$ so that we can integate around the pole. We use the following contour

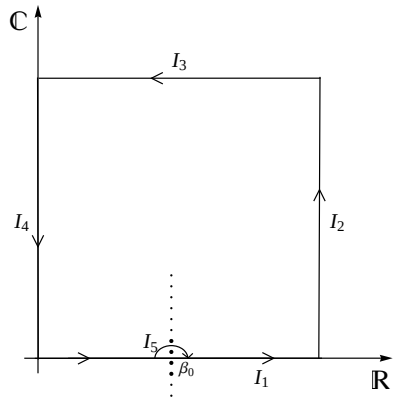

$\gg$ **Evaluating** I_5

Along this path $\zeta = \beta_0 + \delta e^{i\theta} \Rightarrow d\zeta = i\delta e^{i\theta} d\theta$, where $\theta \in [\pi, 0]$

$$I_5 = \lim_{\delta\to 0} \frac{1}{d} \int_C F(\zeta) d\zeta = \lim_{\delta\to 0} \frac{1}{d} \int_\pi^0 \frac{e^{(\beta_0+\delta e^{i\theta})v_+}}{1 - \frac{\delta\epsilon^2}{4} e^{2\beta_0} e^{2\delta e^{i\theta}}} (i\delta e^{i\theta}) d\theta$$
$$= \lim_{\delta\to 0} \frac{1}{d} \left(\frac{4}{\delta\epsilon^2}\right)^{\frac{v_+}{2}} \int_\pi^0 \frac{1 + \delta v_+ e^{i\theta}}{-2\delta e^{i\theta}} (i\delta e^{i\theta}) d\theta = \lim_{\delta\to 0} \frac{i}{d} \left(\frac{4}{\delta\epsilon^2}\right)^{\frac{v_+}{2}} \int_0^\pi \frac{1 + \delta v_+ e^{i\theta}}{2} d\theta$$

Integrating and taking the limit yields

$$I_5 = \frac{1}{d} \frac{i\pi}{2} \left(\frac{4}{\delta\epsilon^2}\right)^{\frac{v_+}{2}} \tag{2.88}$$

Following an analogous procedure as used in section 2.3.2.2 we see that the above result generalizes for $I^\pm$, expanding $v_\pm$ yields

$$\frac{1}{d} \frac{i\pi}{2} \left(\frac{4}{\delta\epsilon^2}\right)^{\frac{v_\pm}{2}} = \frac{1}{d} \frac{i\pi}{2} \left[\left(\frac{4}{\delta\epsilon^2}\right)^{\frac{u+ix}{2d}} + \left(\frac{4}{\delta\epsilon^2}\right)^{\frac{u-ix}{2d}} \right] \tag{2.89}$$

Because everything else was unchanged we can simply add this to (2.87) yielding (showing only the non-conditonal portion for brevity)

$$\begin{aligned}\frac{c}{p}H_{t,y}^{NF} \approx -\frac{\pi}{2d}\Bigg\{&\cot\left[\frac{\pi}{2d}(u+ix)\right]\left(\frac{4}{\delta\epsilon^2}\right)^{\frac{u+ix}{2d}} \\ &+\cot\left[\frac{\pi}{2d}(u-ix)\right]\left(\frac{4}{\delta\epsilon^2}\right)^{\frac{u-ix}{2d}} + i\left[\left(\frac{4}{\delta\epsilon^2}\right)^{\frac{u+ix}{2d}} + \left(\frac{4}{\delta\epsilon^2}\right)^{\frac{u-ix}{2d}}\right]\Bigg\} \\ &+\frac{1}{d}\frac{i\pi}{2}\left[\left(\frac{4}{\delta\epsilon^2}\right)^{\frac{u+ix}{2d}} + \left(\frac{4}{\delta\epsilon^2}\right)^{\frac{u-ix}{2d}}\right]\end{aligned} \tag{2.90}$$

Bringing (2.89) into the { } brackets we see that it exactly cancels the third term, thus reproducing the field derived by Merlin [26] for the lossless case

$$\boxed{\begin{aligned}\frac{c}{p}H_{t,y}^{NF} \approx -\frac{\pi}{2d}\Bigg\{&\cot\left[\frac{\pi}{2d}(u+ix)\right]\left(\frac{4}{\delta\epsilon^2}\right)^{\frac{u+ix}{2d}} + \cot\left[\frac{\pi}{2d}(u-ix)\right]\left(\frac{4}{\delta\epsilon^2}\right)^{\frac{u-ix}{2d}}\Bigg\} \\ +\Bigg\{&\begin{array}{ll} 2e^{u\omega/c}\dfrac{u\cos(\frac{\omega}{c}x)+x\sin(\frac{\omega}{c}x)}{u^2+x^2} & u>0 \\ -\pi N_1\left[\dfrac{\omega}{c}\sqrt{u^2+x^2}\right]\dfrac{\omega u/c}{\sqrt{u^2+x^2}} + \displaystyle\int_{-\frac{\omega}{c}}^{\frac{\omega}{c}}\cos(qx)\cos\left[u\sqrt{\frac{\omega^2}{c^2}-q^2}\right]dq & u<0 \end{array}\end{aligned}} \tag{2.91}$$

For those comparing with [26], it should be noted that we have defined $u \equiv \frac{3}{2}d - z$ while in [26] $u \equiv z - \frac{3}{2}d$ and thus after careful attention to the signs one can see that they are indeed identical expressions.

A typical field profile is shown in Fig. 2.8, and in the plot on the right, like in Firgure 2.3, to avoid the background change and to clearly confirm where the focus occurs we normalize the field by its maximal strength for each value of z, which in the line source geometry ocurs at $x = 0$. A typical field profile in the focal plane is shown in Fig. 2.9. We note that the biggest difference between Fig. 2.9 and Fig. 2.7 is the absence of a decaying envelope of the field, which makes sense due to the lossless transmission. Furthermore in 2.9 we note that the field reaches zero periodically and

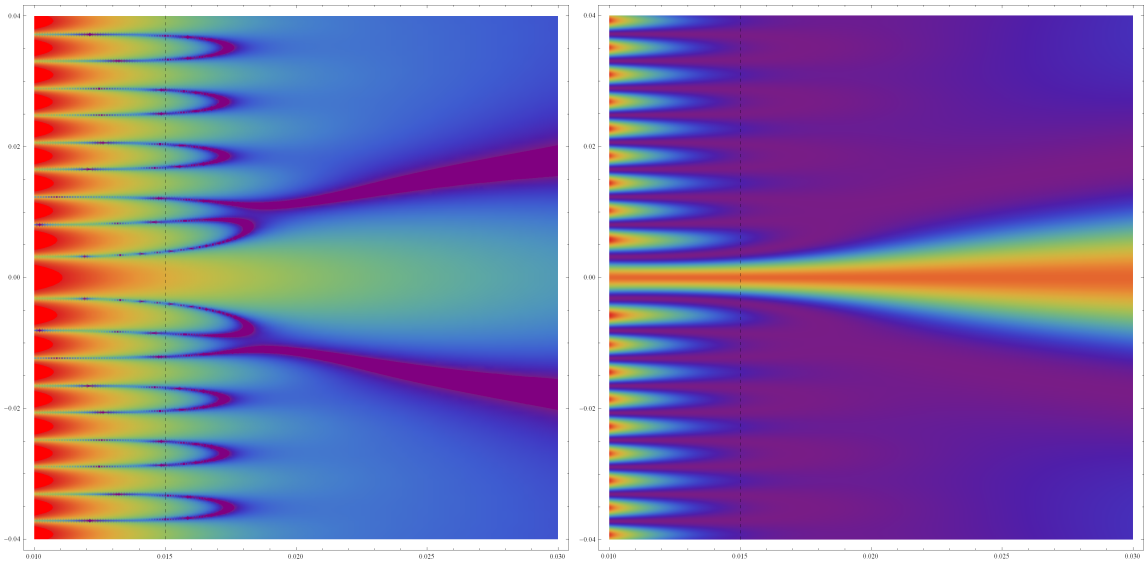

Figure 2.8: Typical field profile as a function of (z, x), the dashed line indicates the focal plane of $z = \frac{3}{2}d$. Left: $\ln|\mathbf{H}_t^{NF}|$ Right: $|\mathbf{H}_t^{NF}(z,x)/\mathbf{H}_t^{NF}(z,0)|^2$

thus does not have the constant offset of the lossy case. We note that these fields are

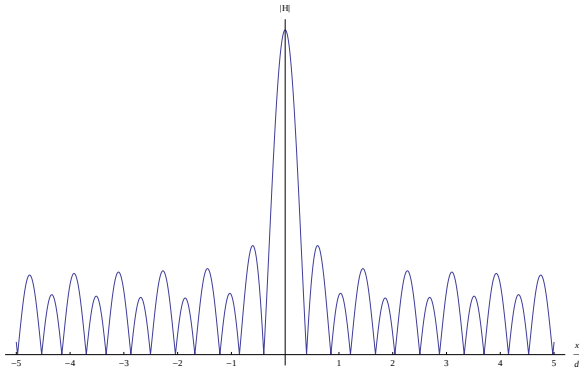

Figure 2.9: Typical field profile of $|\mathbf{H}_t^{NF}|$ in the focal plane of $z = \frac{3}{2}d$

exactly those produced in [26] and [28], and thus we have thoroughly presented the derivation for the results found there. By comparing (2.91) and (2.87) and recalling the discussion of the infinite focii found in section 2.3.3, we see that this field also contains an infinite (albeit still exponentially decreasing in intensity) number of focii. The material losses do not affect this property of a negative refractive index slab.

The effect of (2.89) on the field is essentially only a slight offset of the magnitude.

Therefore (2.32), which was originally derived in [26] for the lossless case (2.91), applies equally well to the lossy case (2.87). Therefore we conlcude that so long as $|\delta\epsilon|$ is constant, the presence of losses does not affect the resolution, only the contrast. We emphasize that for $\delta\epsilon_2 \neq 0$ in order to have constant $|\delta\epsilon|$, $|\delta\epsilon_1|$ must decrease. To derive (2.32) we consider (2.91) or equivalently (2.87) while ignoring the offset term (2.89). We then focus on the first two terms, which are most crucial in determining the resolution, and solve for the first zero in x. We note that solving

$$\cot\left[\frac{\pi}{2d}(u+ix)\right]\left(\frac{4}{\delta\epsilon^2}\right)^{\frac{u+ix}{2d}} + \cot\left[\frac{\pi}{2d}(u-ix)\right]\left(\frac{4}{\delta\epsilon^2}\right)^{\frac{u-ix}{2d}} = 0 \tag{2.92}$$

is equivalent to solving

$$\sin\left(\frac{x}{d}\ln|\delta\epsilon/2|\right) = 0 \tag{2.93}$$

Defining the root of this equation as L_R and doubling to solve for the width of the bottom of the first peak yields (2.32)

$$L_R \approx -\frac{2\pi d}{\ln|\delta\epsilon/2|}$$

2.3.5 Comparison with Numerical Results

To verify the validity of (2.87) and (2.91), which were derived after very long calculations involving numerous small approximations, we calculate the transmitted field numerically as was done for the point source. Equation (2.36) was numerically integrated, again using mathematica, utilizing some of mathematica's built-in abilities to integrate around poles. Fig. 2.10 shows the $|\mathbf{H}_t^{NF}|$ calculated analytically and numerically. The plot on the left, $|\mathbf{H}_t^{NF}|$ calculated analytically, was also shown in Fig. 2.7. The plot on the right, $|\mathbf{H}_t^{NF}|$ calculated numerically, shows exactly the same profile.

We can also carry out this comparison for the lossless case, Fig. 2.11 shows

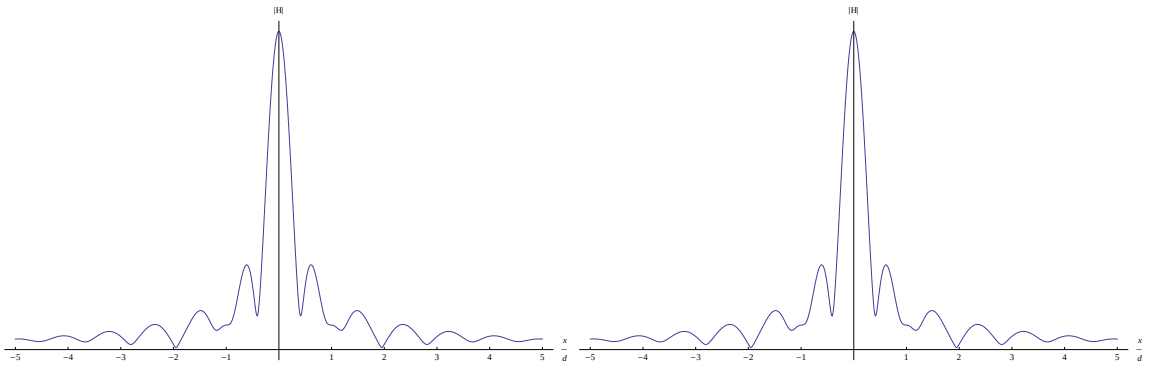

Figure 2.10: Comparison of $|\mathbf{H}_t^{NF}|$ for the lossy case calculated analytically and numerically, Left and Right respetivley

f$|\mathbf{H}_t^{NF}|$ calculated analytically and numerically. The plot on the left, $|\mathbf{H}_t^{NF}|$ calculated

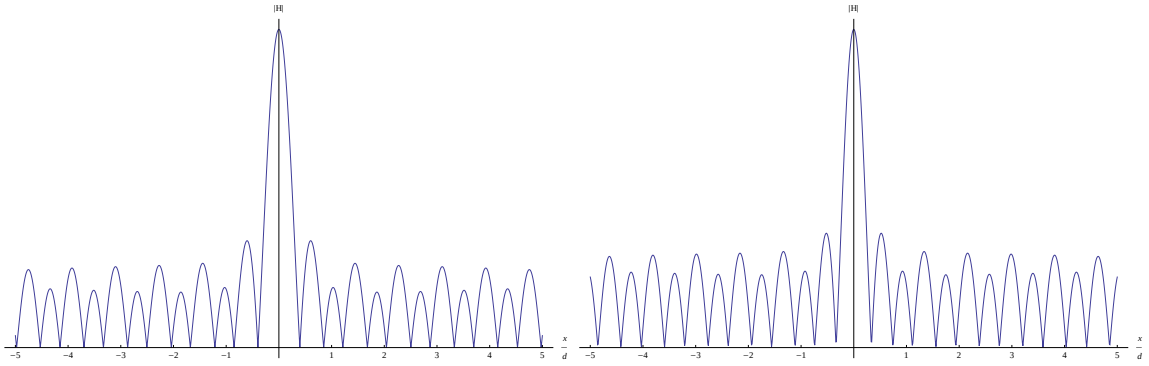

Figure 2.11: Comparison of $|\mathbf{H}_t^{NF}|$ for the lossless case calculated analytically and numerically, Left and Right respetivley

analytically, was also shown in Fig. 2.9. The plot on the right, $|\mathbf{H}_t^{NF}|$ calculated numerically, shows nearly the same profile.

We thus can conclude that our analytical derivation of the transmitted field produced the correct result.

2.4 Conclusion

We have numerically claculated the fields transmitted through a LHM from a point dipole source. We have also analytically derived the transmitted near field through a

LHM for a line of dipole sources. This analysis was carried out to determine the effects of slight deviations in the permitivity and permeability from the impedence matched condition that Pendry used to show perfect resolution [24]. We found that in both geometries the dependence is logarithmic, suggesting that in order to experimentally observe significant improvement over the diffraction limit, in addition to having a sufficently thin material, the deviations from impedence matching are crucial.

Although we have focused here on using slab of LHM to achieve subwavelength focusing, solving for the entire transmitted fields is a meaningful accomplishment. LHMs have only recently begun to be realizable in the lab and are slowly being perfected. Having full solutions for the fields for the very real situation of deviations in the permitivity and permeability will hopefully someday be helpful to those trying to create new and interesting technologies. Only time can tell if LHMs will just be another exotic material for niche applications, or if they will fundamentally change our technology. One thing that is certain is that LHMs will continue to spark the imagination of scientists and engineers for a long time to come.

APPENDICES

APPENDIX A

Code for GaSe Contrast Calculations

This appendix shows the code used for the GaSe contrast analysis shown in Fig. 1.13 and Fig. 1.14. As was explained in Chapter I this calculation is a reproduction of work done by Blake et.al. [19] who created a model based on Fresnel's equations. Their work was for graphene, I have adapted it for use with GaSe. This code is written in Mathematica, it is completely functional and produces the figures using Mathematica 8. Although the program certainly will run if the entire code is put into one cell, it is good Mathematica practice and I recommend that if attempting to use this code you break the code into several cells at logical break points.

```
eSi[en_] := 1.32 + 3.41/(1 - en^2/3.36^2 - (I*0.091*en)/3.36) +
     1.84/(1 - en^2/3.66^2 - (I*0.103*en)/3.66) +
     1.85/(1 - en^2/3.96^2 - (I*0.1*en)/3.96) +
     1.74/(1 - en^2/4.2^2 - (I*0.087*en)/4.2) +
     0.136/(1 - en^2/5.35^2 - (I*0.064*en)/5.35) +
     0.413/(1 - en^2/5.81^2 - (I*0.269*en)/5.81) +
     0.89/(1 - en^2/7.75^2 - (I*0.978*en)/7.75)
eSi1[en_] := Re[eSi[en]]
eSi2[en_] := Im[eSi[en]]
```

```
nSi1[en_] := Sqrt[(1/2)*(eSi1[en] + Sqrt[eSi1[en]^2 + eSi2[en]^2])]
kSi1[en_] := eSi2[en]/(2*nSi1[en])
n3[x_] := nSi1[(1.240700199*10^3)/x] + I*kSi1[(1.240700199*10^3)/x]
n2[\[Lambda]_] :=
 Sqrt[1 + (0.696749*\[Lambda]^2)/(\[Lambda]^2 - (0.0684043*10^3)^2) +
       (0.408218*\[Lambda]^2)/(\[Lambda]^2 - (0.115662*10^3)^2) +
       (0.890815*\[Lambda]^2)/(\[Lambda]^2 - (9.900559*10^3)^2)]
r1[n1_] := (1 - n1)/(1 + n1)
r2[n1_, \[Lambda]_] := (n1 - n2[\[Lambda]])/(n1 + n2[\[Lambda]])
r3[\[Lambda]_] := (n2[\[Lambda]] - n3[\[Lambda]])/(n2[\[Lambda]] +
    n3[\[Lambda]])
\[CapitalPhi]1[n1_, d1_, \[Lambda]_] := (2*Pi*n1*d1)/\[Lambda]
\[CapitalPhi]2[\[Lambda]_, d2_] := (2*Pi*n2[\[Lambda]]*d2)/\[Lambda]
Intensity[n1_, \[Lambda]_, d1_, d2_] :=
   Abs[(r1[n1]*
       E^(I*(\[CapitalPhi]1[n1,
             d1, \[Lambda]] + \[CapitalPhi]2[\[Lambda], d2])) +

      r2[n1, \[Lambda]]/
       E^(I*(\[CapitalPhi]1[n1,
             d1, \[Lambda]] - \[CapitalPhi]2[\[Lambda], d2])) +

      r3[\[Lambda]]/
       E^(I*(\[CapitalPhi]1[n1,
             d1, \[Lambda]] + \[CapitalPhi]2[\[Lambda], d2])) +

      r1[n1]*r2[n1, \[Lambda]]*r3[\[Lambda]]*
```

```
       E^(I*(\[CapitalPhi]1[n1, d1, \[Lambda]] -
                    \[CapitalPhi]2[\[Lambda], d2])))/
         (E^(I*(\[CapitalPhi]1[n1,
            d1, \[Lambda]] + \[CapitalPhi]2[\[Lambda], d2])) +
            (r1[n1]*r2[n1, \[Lambda]])/
       E^(I*(\[CapitalPhi]1[n1,
             d1, \[Lambda]] - \[CapitalPhi]2[\[Lambda], d2])) +
            (r1[n1]*r3[\[Lambda]])/
       E^(I*(\[CapitalPhi]1[n1,
             d1, \[Lambda]] + \[CapitalPhi]2[\[Lambda], d2])) +


      r2[n1, \[Lambda]]*r3[\[Lambda]]*
       E^(I*(\[CapitalPhi]1[n1,
             d1, \[Lambda]] - \[CapitalPhi]2[\[Lambda], d2])))]^2
Contrast[n1_, \[Lambda]_, d1_, d2_] :=
   (Intensity[1, \[Lambda], d1, d2] -
    Intensity[n1, \[Lambda], d1, d2])/
     Intensity[1, \[Lambda], d1, d2]


Needs["PlotLegends`"]
Plot[{Abs[Contrast[Sqrt[-((0.05466*(10^3)^4)/\[Lambda]^4) +
             (0.48605*(10^3)^2)/\[Lambda]^2 + 7.8902 -
      0.000824*(1/10^3)^2*\[Lambda]^2 -
             2.73*^-6*(1/10^3)^4*\[Lambda]^4], \[Lambda], 5, 285]],
     Abs[Contrast[Sqrt[-((0.05466*(10^3)^4)/\[Lambda]^4) +
             (0.48605*(10^3)^2)/\[Lambda]^2 + 7.8902 -
      0.000824*(1/10^3)^2*\[Lambda]^2 -
```

```
            2.73*^-6*(1/10^3)^4*\[Lambda]^4], \[Lambda], 10, 285]],
    Abs[Contrast[Sqrt[-((0.05466*(10^3)^4)/\[Lambda]^4) +
            (0.48605*(10^3)^2)/\[Lambda]^2 + 7.8902 -
     0.000824*(1/10^3)^2*\[Lambda]^2 -
            2.73*^-6*(1/10^3)^4*\[Lambda]^4], \[Lambda], 15, 285]],
    Abs[Contrast[Sqrt[-((0.05466*(10^3)^4)/\[Lambda]^4) +
            (0.48605*(10^3)^2)/\[Lambda]^2 + 7.8902 -
     0.000824*(1/10^3)^2*\[Lambda]^2 -
            2.73*^-6*(1/10^3)^4*\[Lambda]^4], \[Lambda], 30,
   285]]}, {\[Lambda], 410, 740},
  PlotRange -> All, AxesOrigin -> {410, 0},
  PlotLegend -> {"d = 5 nm", "d = 10 nm", "d = 15 nm", "d = 30 nm"},
  LegendShadow -> None, ImageSize -> Large,
  LegendPosition -> {0.5, 0}, LegendSize -> 0.5, PlotStyle -> Thick,
  AxesLabel -> {"\[Lambda] (nm)", "|Contrast|"}]

ShowLegend[
 DensityPlot[Contrast[Sqrt[-((0.05466*(10^3)^4)/\[Lambda]^4) +
          (0.48605*(10^3)^2)/\[Lambda]^2 + 7.8902 -
    0.000824*(1/10^3)^2*\[Lambda]^2 -
          2.73*^-6*(1/10^3)^4*\[Lambda]^4], \[Lambda], 0.8, d], {d,
  0, 350},
    {\[Lambda], 410, 740}, ColorFunction -> "BlueGreenYellow",
    PlotPoints -> 200, FrameLabel -> {"d (nm)", "\[Lambda] (nm)"}],
  {ColorData["BlueGreenYellow"][1 - #1] & , 10, " High", "Low",
    LegendPosition -> {1.1, -0.4}, LegendShadow -> None,
    LegendBorder -> None}]
```

APPENDIX B

Integral Identities

The following definite integral identities involving Bessel functions were used:

$$\int_0^{2\pi} e^{iqr\cos\theta} d\theta = 2\pi J_0(qr) \tag{B.1}$$

$$\int_0^{2\pi} \cos\theta e^{iqr\cos\theta} d\theta = 2\pi i J_1(qr) \tag{B.2}$$

$$\int_0^{2\pi} \cos(2\theta) e^{iqr\cos\theta} d\theta = -2\pi J_2(qr) \tag{B.3}$$

$$\int_0^{2\pi} \sin\theta e^{iqr\cos\theta} d\theta = 0 \tag{B.4}$$

$$\int_0^{2\pi} \sin(2\theta) e^{iqr\cos\theta} d\theta = 0 \tag{B.5}$$

BIBLIOGRAPHY

BIBLIOGRAPHY

[1] K. S. Novoselov, et al, "Electric field effect in atomically thin carbon films," Science **306**, 666 (2004).

[2] W. Choi, I. Lahiri, R. Seelaboyina, and Y. Kang, "Synthesis of Graphene and Its Applications: A Review," Crit. Rev. Sol. Stat. and Mat. Sci. **1**, 52 (2010).

[3] A. K. Geim and A. H. MacDonald, "Graphene: Exploring Carbon Flatland," Phys. Today **8**, 35 (2007).

[4] A. H. Castro Neto, et al, "The electronic properties of graphene," Rev. Mod. Phys. **81**, 109 (2009).

[5] A. K. Geim, "Graphene Status and Prospects," Science **324**, 1530 (2009).

[6] P. Harrison, *Quantum Wells, Wires, and Dots* (John Wiley & Sons, 3 ed 2009).

[7] S. I. Pekar, "Dispersion of light in the exciton absorption region of crystals," Sov. Phys. JETP **7**, 813 (1958).

[8] R. S. Knox, *Theory of Excitons* (Academic Press, 1963). "

[9] M. Fox, *Optical Properties of Solids* (Oxford University Press, 2001).

[10] R. Dingle, "Confined carrier quantum states in ultrathin semiconductor heterostructures," Adv. in Sol. Stat. Phys. **15**, 21 (1975).

[11] N. C. Fernelius, "Properties of gallium selenide single crystal," Prog. Crys. Grow. and Char. Mat. **28**, 275 (1994).

[12] K. Ueno, H. Abe, K. Saiki, and A. Koma, "Heteroepitaxy of Layered Semiconductor GaSe on a GaAs(111)B Surface," Jpn. J. Appl. Phys. **30**, L1352 (1991).

[13] X. H. Zhu, Z. R. Wei, Y. R. Jin, A. P. Xiang, "Growth and characterization of a PbI2 single crystal used for gamma ray detectors," Cryst. Res. Technol. **42**, 456 (2007).

[14] V. Grasso, *Electronic structure and electronic transitions in layered materials* (Springer, 1986).

[15] M. Kepinska, Z. Kovalyuk, R. Murri, M. Nowak, "Temperature dependence of optical energy gap of GaSe," Wide Bandgap Layers, 2001. Abstract Book. 3rd International Conference on Novel Applications of, 146 (2001).

[16] G. Antonioli, D. Bianchi, V. Canevari, U. Emiliani and P. Podini, "Optical properties and electron-phonon interaction in GaSe," Il Nuovo Cimento. B **54**, 211 (1979).

[17] R. Ahuja, H. Arwin, A. Ferreira da Silva, C. Persson, J. M. Osorio-Guillen, J. Souza de Almeida, C. Moyses Araujo, E. Veje, N. Veissid, C. Y. An, I. Pepe, and B. Johansson, "Electronic and optical properties of lead iodide," J. Appl. Phys. **92**, 7219 (2002).

[18] Ch. Gahwiller, G. Harbeke, "Excitonic Effects in the Electroreflectance of Lead Iodide," Phys. Rev. **185**, 1141 (1969).

[19] P. Blake, E. W. Hill, A. H. Castro Neto, K. S. Novoselov, D. Jiang, R. Yang, T. J. Booth, and A. K. Geim, "Making graphene visible," Appl. Phys. Lett. **91**, 063124 (2007).

[20] A. Mechler, J. Kopniczky, J. Kokavecz, A. Hoel, C. G. Granqvist, and P. Heszler, "Anomalies in nanostructure size measurements by AFM," Phys. Rev. B **72**, 125407 (2005).

[21] D. R. Smith, J. B. Pendry, and M. C. K. Wiltshire, "Metamaterials and Negative Refractive Index," Science **305**, 788 (2004).

[22] V. M. Shalaev, "Optical negative-index metamaterials," Nat. Photonics **1**, 41 (2007).

[23] N. M. Litchinitser and V. M. Shalaev, "Metamaterials: transforming theory into reality," J. Opt. Soc. Am. B **26**, B161 (2009).

[24] J. B. Pendry, "Negative Refraction Makes a Perfect Lens," *Phys. Rev. Lett.***85**, 3966 (2000).

[25] V. G. Veselago,"The electrodynamics of substances with simultaneously negative values of ϵ and μ," Sov. Phys. Usp. **10**, 509 (1968).

[26] R. Merlin, "Analytical solution of the almost-perfect-lens problem," Appl. Phys. Lett. **84**, 1290 (2004).

[27] D. R. Smith, D. Schurig, M. Rosenbluth, S. Schultz, S. A. Ramakrishna, and J. B. Pendry, "Limitations on subdiffraction imaging with a negative refractive index slab, Appl. Phys. Lett. **82**, 1506 (2003).

[28] R. Merlin, "Radiationless Electromagnetic Interference: Evanescent-Field Lenses and Perfect Focusing," Science **317**, 927 (2007).

[29] R. Marqus and J. Baena, "Effect of losses and dispersion on the focusing properties of left-handed media," Microw. Opt. Technol. Lett. **41**, 290 (2004).

[30] B. Zhang and J. B. Khurgin, "Eigen mode approach to the sub-wavelength imaging with surface plasmon polaritons," Appl. Phys. Lett. **98**, 26310 (2011).

[31] C. J. Zapata-Rodriguez, D. Pastor, and J. J. Miret, "Three-dimensional point spread function and generalized amplitude transfer function of near-field flat lenses," Appl. Opt. **49**, 5870 (2010).

[32] G. D'Aguanno, N. Mattiucci, and M. J. Bloemer, "Influence of losses on the superresolution performances of an impedance-matched negative-index material," J. Opt. Soc. Am. B **25**, 236 (2008).

[33] B. Gralak and S. Guenneau, "Transfer matrix method for point sources radiating in classes of negative refractive index materials with 2n-fold antisymmetry," Wave Random Complex **17**, 581 (2007).

[34] V. A. Podolskiy, N. A. Kuhta, and G. W. Milton, "Optimizing the superlens: Manipulating geometry to enhance the resolution," Appl. Phys. Lett. **87**, 231113 (2005).

[35] L. Zhou and C. T. Chan, "Vortex-like surface wave and its role in the transient phenomena of meta-material focusing," Appl. Phys. Lett. **86**, 1011041 (2005).

[36] V. A. Podolskiy and E. E. Narimanov, "Near-sighted superlens," Opt. Lett. **30**, 75 (2005).

[37] K. Aydin, I. Bulu, and E. Ozbay, "Subwavelength resolution with a negative-index metamaterial superlens," Appl. Phys. Lett. **90**, 254102 (2007).

[38] M. W. Feise, Y. S. Kivshar, "Sub-wavelength imaging with a left-handed material flat lens," Phys. Lett. A **334**, 326 (2005).

[39] J. B. Pendry and S. A. Ramakrishna, "Focusing light using negative refraction," J. Phys.: Condens. Matter **15**, 6345 (2003).

[40] N. Fang and X. Zhang, "Imaging properties of a metamaterial superlens," App. Phys. Lett. **82**, 161 (2003).

[41] Z. Ye, "Optical transmission and reflection of perfect lenses by left handed materials," *Phys. Rev. B***67**,193106 (2003).

[42] L. Chen, S. He, and L. Shen, "Finite-Size Effects of a Left-Handed Material Slab on the Image Quality," *Phys. Rev. Lett.***92**, 107404 (2004).

[43] A. Husakou and J. Herrmann, "Superfocusing of light below the diffraction limit by photonic crystals with negative refraction," Opt. Express **12**, 6491 (2004).

[44] V. N. Kissel and A. N. Lagarkov, "Superresolution in left-handed composite structures: from homogenization to a detailed electrodynamic description, *Phys. Rev. B***72**, 085111-085119 (2005).

[45] J. T. Shen and P. M. Platzman, "Near field imaging with negative dielectric constant lenses," Appl. Phys. Lett. **80**, 3286 (2002).

[46] S. A. Cummer, "Simulated causal subwavelength focusing by a negative refractive index slab," Appl. Phys. Lett. **82**, 1503 (2003).

[47] G. W. Milton, N. P. Nicorovici, R. C. McPhedran, and V. A. Podolskiy, "A proof of superlensing in the quasistatic regime, and limitations of superlenses in this regime due to anomalous localized resonance," Proc. R. Soc. A **461**, 3999 (2005).

[48] M. Born and E. Wolf, *Principles of Optics* (Cambridge, 7 ed. 2002).